

NASA Contractor Report 189139

~~E6478~~
1-15-93

E-7428

Micro Electric Propulsion Feasibility

Graeme Aston and Martha Aston
Electric Propulsion Laboratory
Tehachapi, California

November 1992

NASA

"SBIR Rights Notice"

These SBIR data are furnished with SBIR rights under NASA Contract NAS3-26062. For a period of two years after acceptance of this report the Government agrees to use these data for Government purposes only, and it shall not be disclosed outside the Government (including disclosure for procurement purposes) during such period without permission of the Electric Propulsion Laboratory, Inc., except that, subject to the foregoing use and disclosure prohibitions, such data may be disclosed for use by support contractors to the Electric Propulsion Laboratory, Inc. After the aforesaid two year period, the Government has a royalty free license to use, and to authorize others to use on its behalf, these data for Government purposes, but is relieved of all disclosure prohibitions and assumes no liability for unauthorized use of these data by third parties.

MICRO ELECTRIC PROPULSION FEASIBILITY

Graeme Aston and Martha Aston
Electric Propulsion Laboratory
Tehachapi, California 93561

INTRODUCTION

Miniature, 50 kg class, strategic satellites intended for extended deployment in space require an on-board propulsion capability to perform needed attitude control adjustments and drag compensation maneuvers. Even on such very small spacecraft, these orbit maintenance functions can be significant and result in a substantial propellant mass requirement. Development of advanced propulsion technology could reduce this propellant mass significantly, and thereby maximize the payload capability of these spacecraft. In addition, spacecraft maneuverability could be enhanced and/or multi-year mission lifetimes realized. These benefits cut spacecraft replacement costs, and reduce services needed to maintain the launch vehicles.

For SDIO brilliant pebble spacecraft, a miniaturized hydrazine propulsion system provides both boost and divert thrust control.^{1,2} This type of propulsion system is highly integrated and is capable of delivering large thrust levels for short time periods. However, orbit maintenance functions such as drag make-up require only very small velocity corrections. Using the boost and/or divert thrusters for these small corrections exposes this highly integrated propulsion system to continuous on/off cycling and thereby increases the risk of system failure. Furthermore, since drag compensation velocity corrections would be orders of magnitude less than these thrusters were designed to deliver, their effective specific impulse would be expected to be lower when operated at very short pulse lengths. The net result of these effects would be a significant depletion of the on-board hydrazine propellant supply throughout the mission, and a reduced propulsion system reliability, both of which would degrade the interceptor usefulness.

In addition to SDIO brilliant pebble spacecraft, comparably small spacecraft can be anticipated for other future strategic defense applications such as surveillance and communication. For such spacecraft, high capability and reliability, minimal detectability and low cost are requirements. All these miniature spacecraft share a common characteristic: because of their on-board electronic equipment they have, by design, solar array power systems which can provide continuous power levels of order 50 - 100 W. In a relative sense, such spacecraft are power rich when compared to other larger spacecraft. This power rich situation is offset by very tight mass budgets, which make reductions in propellant mass requirements a key issue in meeting overall spacecraft minimum mass goals. In principle, power rich and propellant poor brilliant pebbles class spacecraft can benefit from using high specific impulse electric propulsion to reduce chemical propellant mass requirements. However, at power levels of order 50 W, arcjets cannot be made to function, ion thrusters are too complex and heavy, and resistojets have too low a specific impulse.

Recognizing these capability limitations in existing electric propulsion technology, the SDIO/IST sponsored the Phase I SBIR Micro Electric Propulsion (MEP) thruster study described in this report. The objective of this study was to examine the feasibility of developing a very simple, low mass and small volume, electric thruster for operation on hydrazine at less than 100 W of input power. The feasibility of developing such a MEP thruster was successfully demonstrated by EPL by the discovery of a novel plasma acceleration process. The following sections in this report summarize the approach, test results and major accomplishments of this proof-of-concept program.

TEST FACILITIES

Definitive proof-of-concept tests were performed during this program which identified several key parameters important to the development of a MEP thruster. These tests were performed using existing EPL test facilities and support equipment.

Vacuum Chamber and Pumps

All MEP thruster and component testing was performed in a non-magnetic stainless steel vacuum chamber that was 1.83 m long and 0.59 m in dia. Each end of this chamber was fitted with hinged access doors which allowed for rapid experimental test set-up and removal. High vacuum pumping for this test chamber was provided by a Varian HS-20 diffusion pump which had a nominal pumping speed of approximately 17,000 liters/sec. on air. Dow Corning 702 silicone diffusion pump oil was used in this pump to maintain a relatively low backstreaming rate while ensuring a high throughput. A Kinney KMBD-400 Roots blower was used to back the diffusion pump, and this blower was in turn backed by a Kinney KT-150 mechanical roughing pump. This vacuum test facility was capable of ultimate pressures of 1×10^{-6} Torr with no gas load. During the course of MEP thruster testing, typical background pressures were $1.5 - 2.0 \times 10^{-5}$ Torr. However, during parametric flow testing, MEP thruster operation was sustained with a background pressure as low as 8×10^{-6} Torr and as high as 1×10^{-4} Torr.

Power Supplies

Figure 1 shows the laboratory power supplies used for MEP thruster testing. Heater power was provided by a simple ferroresonant D.C. power supply which could deliver a maximum current of 17.0 A to the MEP thruster heater. This power supply was operated in the current limited mode. Current adjustment was provided by a rheostat in parallel with the heater which served as a current bleed path to vary the heater current as required. Heater current regulation was approximately 3%. Arc discharge power to the anode(s) was provided by standard laboratory voltage and current regulated power supplies which were operated in the current regulated mode. Both a Harrison and Trygon power supply were used for this purpose, and most of the testing occurred with the latter power supply which had a compliance voltage of 42 V and a maximum current capability of 15.0 A. Current regulation for the Trygon Model RS40-15B power supply was approximately 0.1%.

The high voltage power supply shown in Fig. 1 performed several functions throughout this test program. Although most MEP thruster geometries required 40 V or less to initiate an anode discharge, some test configurations required up to 600 V of applied anode voltage before breakdown occurred. Similarly, during low flow rate parametric testing, anode voltage levels would exceed 42 V and this high voltage power supply was used to

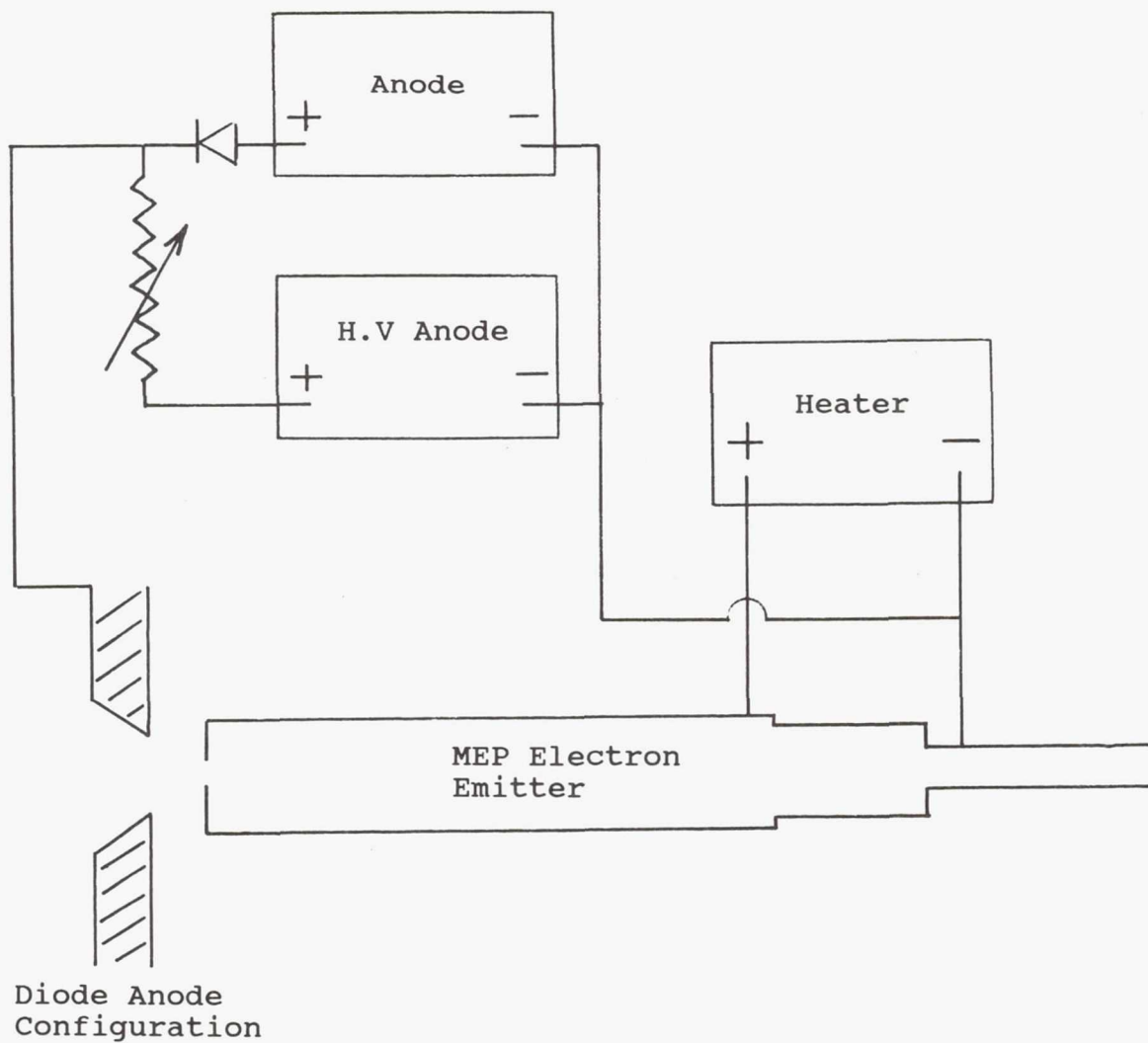


Fig. 1
MEP Thruster Power Supply System

sustain MEP thruster operation at these higher anode voltage levels. Current regulation for this EPL fabricated high voltage supply was approximately 5%

Flow System and Calibration

A 33% N₂/67% H₂ gas mixture was used to simulate MEP thruster operation with hydrazine propellant. This gas mixture was procured in a Linde ultra plus grade with a minimum purity of 99.9995%. Figure 2 details the propellant flow system used for all MEP thruster testing with this gas mixture. As noted in this figure, mass flow calibration tests were performed by monitoring the pressure drop in an accurately known volume. These volume bleed down tests were then compared with the metered flow rate shown on the Teledyne Hastings-Raydist electronic flow rate controller, which had been factory calibrated for direct reading with the simulated hydrazine gas mixture. Figure 3 plots the results of these flow rate calibration tests, and also shows that the indicated flow controller readings were within the $\pm 3\%$ uncertainty of the volume bleed down flow rate measurements.

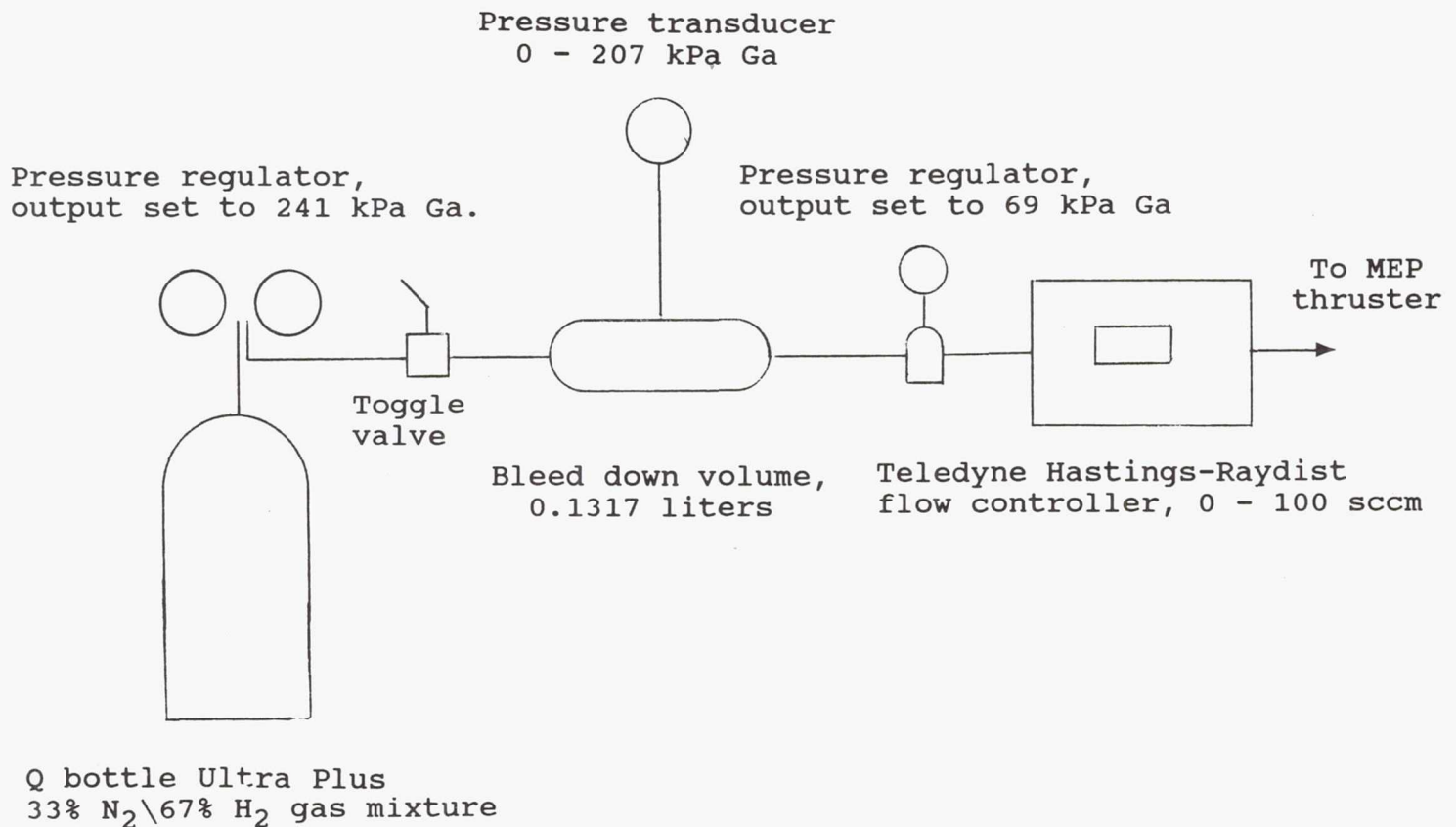


Fig. 2
Propellant Mass Flow Control System

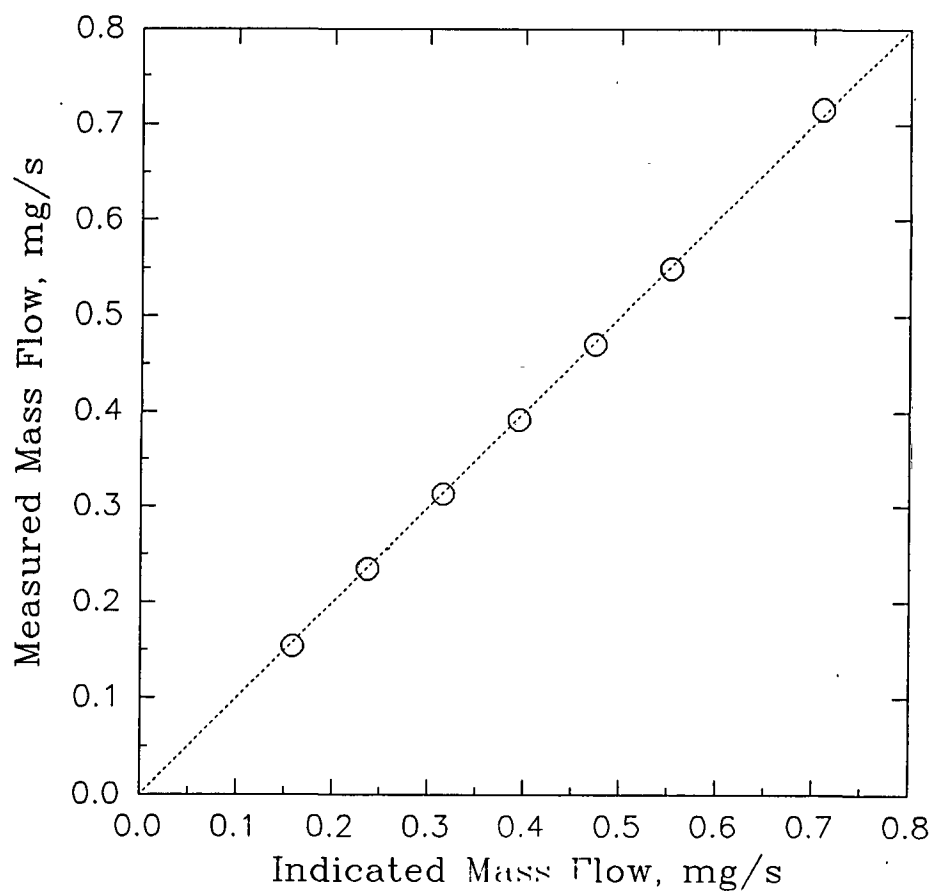


Fig. 3
Electronic Flow Controller Calibration Results

DIAGNOSTICS AND DATA ANALYSIS

A sponsor requirement for this Phase I investigation was that MEP thruster operation be characterized in terms of thrust, specific impulse and efficiency. EPL satisfied this requirement by assembling a momentum probe system using technology previously developed at EPL.^{3,4}

Momentum Probe Design

The momentum probe is a sensitive diagnostic that has been developed by EPL to measure thrust density in a very low thrust electric propulsion engine exhaust plume. Direct thrust stand measurement of low thrust electric propulsion thrusters is very difficult, and expensive in terms of instrumentation fabrication costs, and set-up and calibration time.^{5,6} An early attempt at using an indirect plume momentum measurement approach was made using a stationary, large area mica torsion pendulum target.⁷ The EPL momentum probing system extends these earlier techniques by incorporating an extremely sensitive momentum detecting target onto a translating carriage so that total integrated thrust, in addition to plume expansion features, can be measured.

Figure 4 shows a schematic representation of the main features of the momentum probe system as applied by EPL to the measurement of MEP thruster performance parameters. As shown in Fig. 4, the plume particles pushing on the target cause the target to move, thereby moving the thin needle away from its null position as detected by a simple optical sensor. The needle is returned to its null position by rotating the chain length extension spool and reeling out the chain until the dangling chain mass is sufficient to exactly oppose the thrusting force.

The optical sensor is an EPL design and consists of a light emitting diode, a thin slit and a CdS photocell. Passage of this needle away from this null position, which is to shadow the slit, increases the photocell current. This increase in photocell current is noted by a precision current meter. A flexible shaft, controlled by an operator external to the vacuum system, is used to unwind the chain take-up spool to let out more chain to counteract the impinging plume particle force and bring the needle back to its null (minimum photocell current) position.

Both mica and titanium were used by EPL for the momentum probe target material during testing of the MEP thruster. Use of mica resulted in an insulated target. With the titanium target, care was taken to ensure that there was a low resistance path (less than 1.0 ohm) connection between the target and the grounded vacuum facility. No difference in momentum probe response was noted with either target material when used to probe the MEP thruster plume at identical operating conditions. This result suggested that no significant charge accumulation occurred on either target. All of the initial MEP thruster test data described in this report were obtained using a mica target, while a grounded titanium target was used for the majority of the

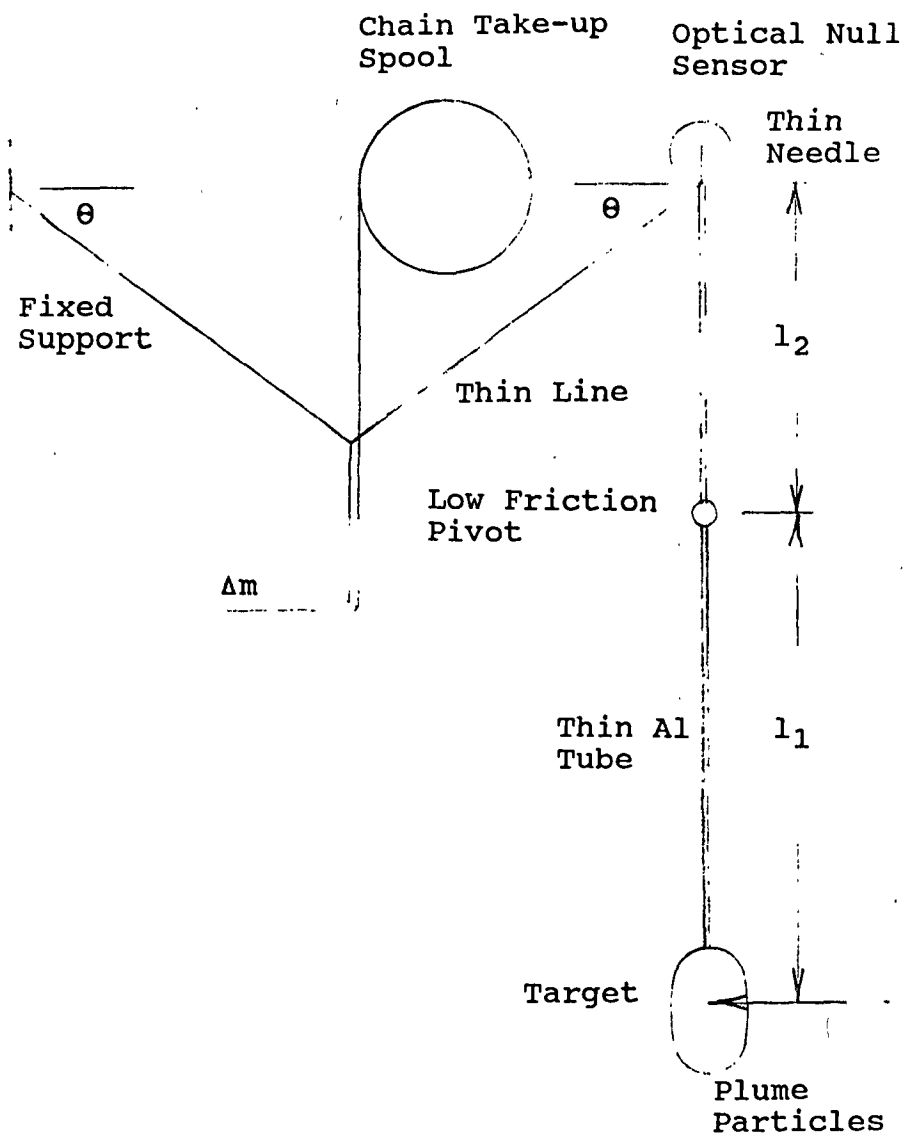


Fig. 4
Momentum Probe Operating Principle

geometric parametric tests.

Probe Set-up

Figures 5a and 5b show the momentum probe system mounted inside the vacuum test facility. As noted in these figures, the momentum probe was attached to a support stand which was in turn attached to a screw type translation carriage. The translation lead screw was driven by a reversible A.C. motor with probe position sensed by a precision, pulley threaded, ten-turn potentiometer. The entire momentum probing system was mounted on an aluminum plate which was located immediately above the diffusion pump entrance at the center of the vacuum tank. This location was determined to have the least amount of mechanical vibration. In addition, vibration isolation pads (as shown in Fig. 5b) were used to further reduce any mechanical coupling between the vacuum test facility and the momentum probing system.

Figures 6a and 6b show details of the optical sensor and chain take-up spool mechanism. Gold was used for the chain since its high density permitted a finer chain to be used, which in turn increased the thrust measurement resolution. EPL experience has shown that a single turn chain take-up spool is preferable since it prevents chain length uncertainties which can occur if the chain inadvertently loops over itself. A precision potentiometer, attached directly to the chain take-up spool, recorded the increments in chain length that were unwound. As noted in Figs. 6a and 6b, the slit was formed from two razor blades, the needle was an ordinary sewing needle, and the low friction pivot was a standard D'Arsonval meter movement which was removed from its meter housing and permanent magnet pole piece fixture. Finally, a human hair was used to form the thin connecting line between the needle, chain, and fixed support. The same hair was used throughout the test program. It should be noted from Figs. 4, 5 and 6, that the entire mechanical linkage system comprising the momentum probe was always placed well out of the MEP thruster plume to minimize heating and/or contamination effects.

Figures 7a and 7b show details of the mica and grounded titanium momentum probe system plume targets that were used during this investigation. Target area was varied from 2.2 to 5.5 cm² depending upon the plume expansion characteristics of the particular MEP thruster geometry being investigated. In general, the chosen target area was a compromise between thrust signal strength and plume spatial resolution. Most of the MEP thruster geometry parametric testing was performed with a 2.51 cm² target area.

The momentum probing system was surprisingly robust and was unaffected by the approximately fifty times the MEP thruster, and attached momentum probing system pallet, was removed from the vacuum system for inspection and/or modification. The mechanical simplicity of the momentum probing system belies the fine sensitivity of the apparatus. Target thrust readings were

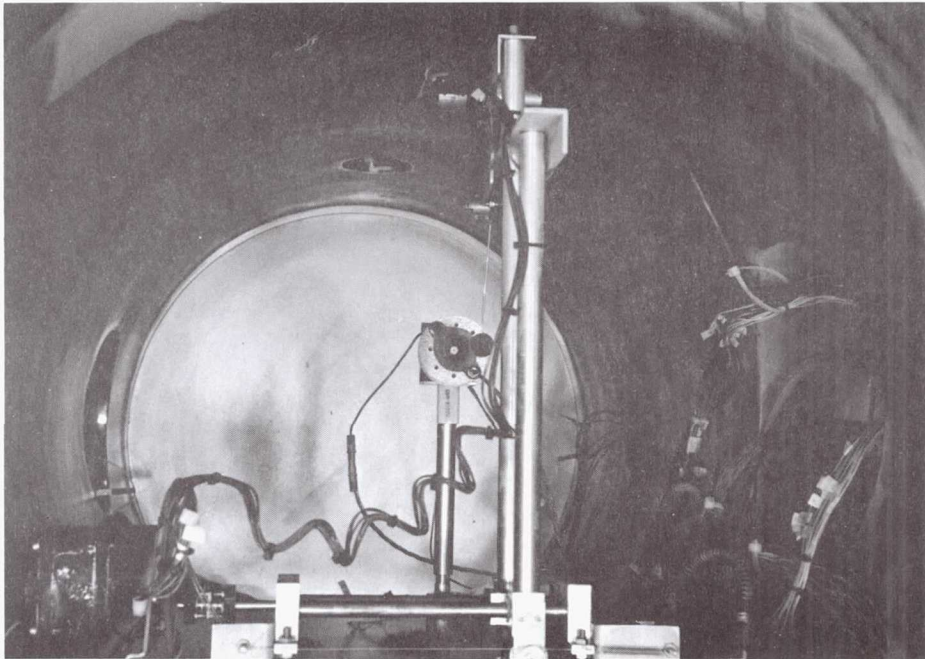


Fig. 5a
Translating Momentum Probe System Mounted in Vacuum Test Facility

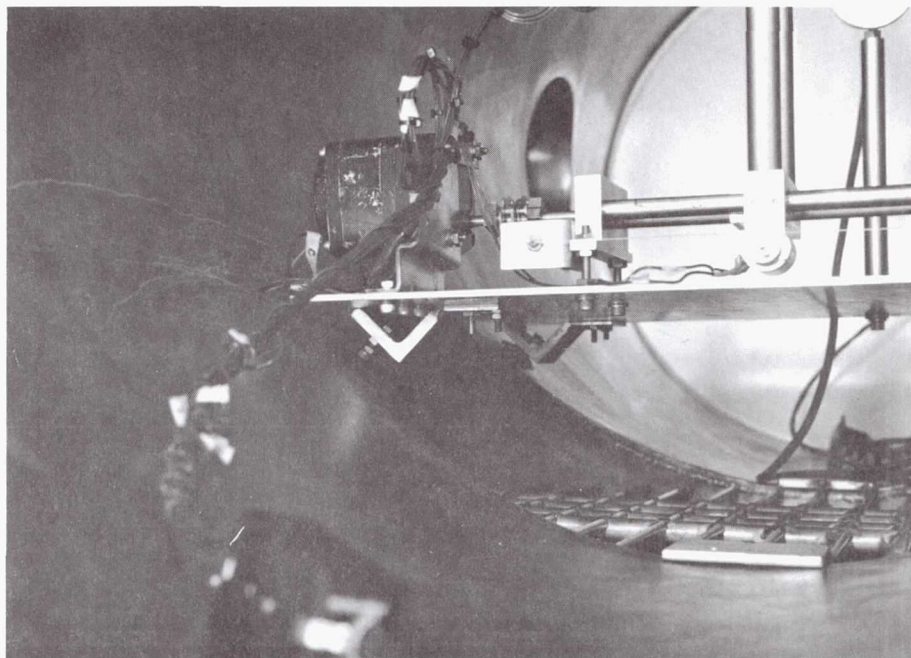


Fig. 5b
Detail of Probe Translating Mechanism and Vibration Isolation
Mounting Pads

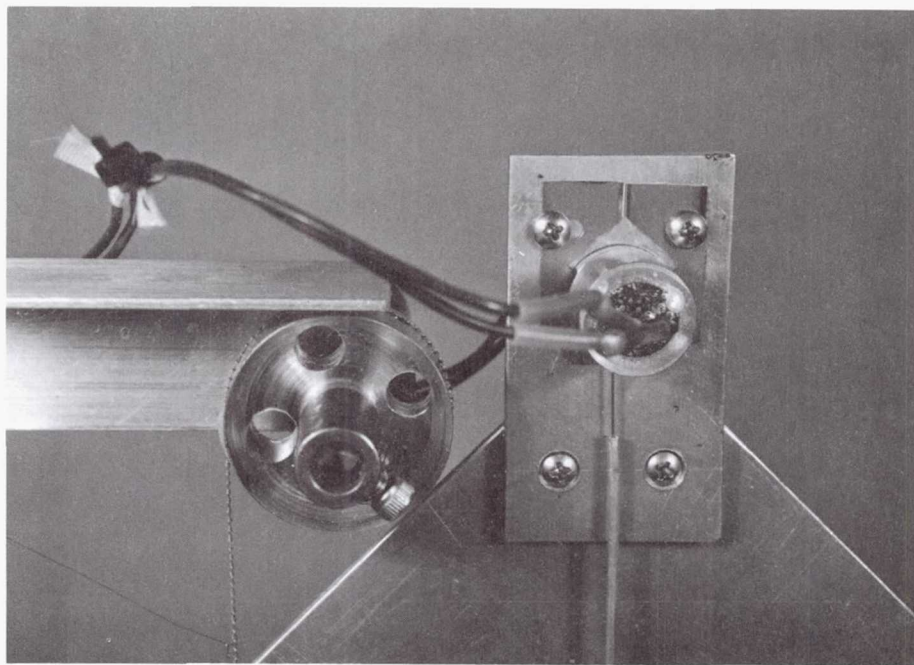


Fig. 6a
Front View of Momentum Probe Optical Null Sensor and Chain Take-
up Spool

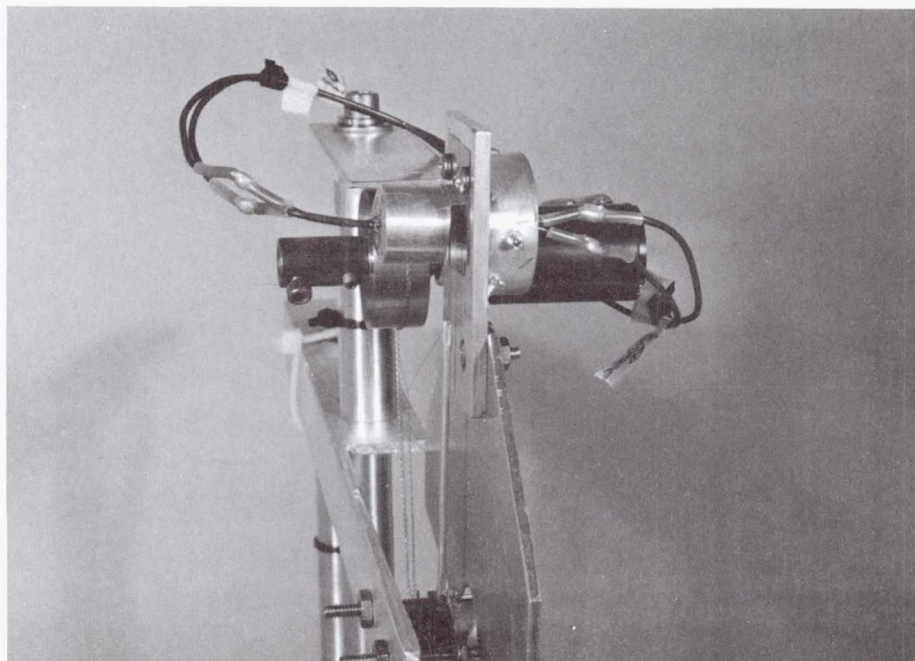


Fig. 6b
Side View of Fig. 6a Showing Low Friction Pivot Mechanism and
Chain length sensing Potentiometer

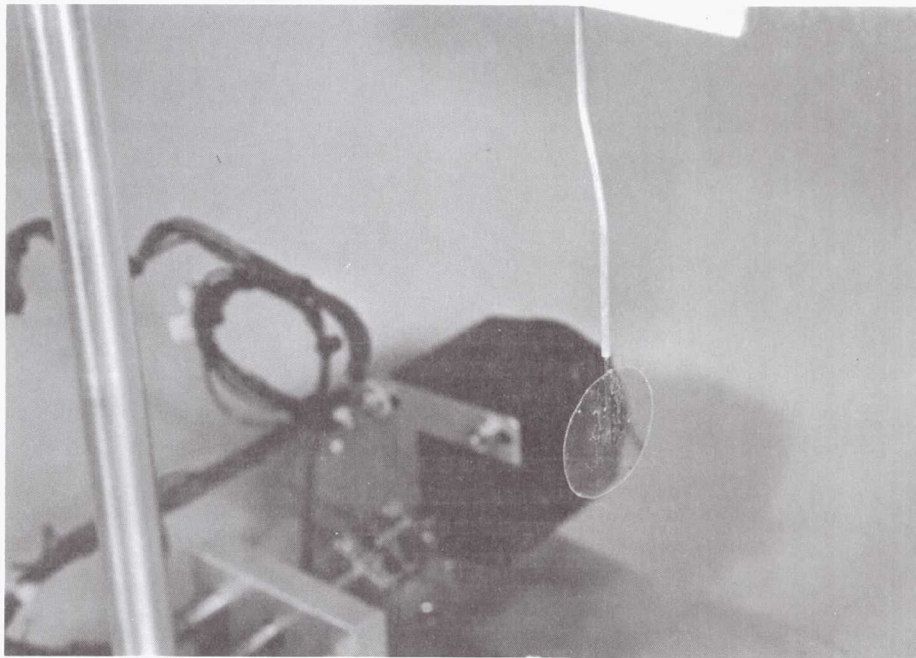


Fig. 7a
Typical Mica Target

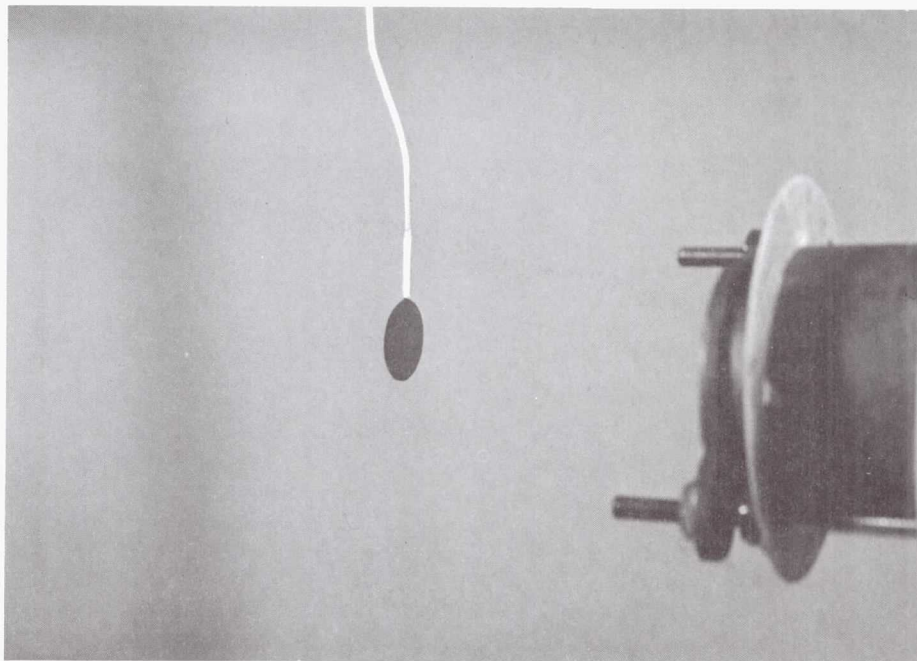


Fig. 7b
Typical Grounded Titanium Target

routinely obtained with a measurement resolution of 200 nanoNewtons.

Data Collection and Analysis

Figure 8 lists the equations used to determine MEP thruster performance. The thrust term, T , noted in these equations refers to the actual thrust as measured by the momentum probe target (ie. the actual force required to restore the target to its null, equilibrium position). Scanning the probe through the MEP thruster exhaust plume, and measuring thrust density at several locations normal to the plume axis, resulted in a thrust density profile which was then integrated to give total thrust. Due to space limitations inside the vacuum test facility, the momentum probe scanned from the extreme edge of the plume, through the plume centerline to a region approximately 2 cm past the centerline where the measured thrust density was usually decreasing rapidly. Typically, this probing envelope included a total probe translation distance of 11.0 cm and encompassed thrust density measurements out to a plume divergence half angle of 45 deg.

Usually, eleven thrust density measurements were taken as the momentum probe was translated through the MEP thruster plasma plume. Approximately 20 - 30 sec. was required to obtain each thrust density measurement, which resulted in about a five minute period to characterize a particular thruster operating condition. The operating characteristics of the MEP thruster were such that operation was extremely stable. Furthermore, no drifts, or time dependent variations were noted with the momentum probing system which would have caused significant errors during the course of a plume thrust density measurement sequence.

A full thrust density profile was obtained for analysis by assuming symmetry about the plume centerline and using reflected plume thrust density data points to form a complete profile. This profile was analyzed by first using a cubic spline to interpolate between data points, and then integrating over annular plume thrust density segments using a modified trapezoidal method.

Once the total plume thrust was obtained, the equations listed in Fig. 8 were solved to obtain the desired MEP thruster performance parameters. In practice, each MEP thruster geometry investigated during this program was operated over a test matrix which usually involved first determining the cold gas flow plume thrust density characteristics, heater and plasma discharge current and voltage characteristics for various flow rates, and then plume thrust density measurements corresponding to different MEP thruster operating conditions. At the completion of these measurements, the data were analyzed using a computer program which performed the above described integrations and solved the equations in Fig. 8. This information was then used to determine MEP thruster design changes appropriate for further testing.

$$T = \frac{l_2}{l_1} \left[\frac{\Delta m}{2 \tan \theta} \right]$$

$$I_{sp} = \frac{T}{\dot{m}g}$$

$$\eta = \frac{I_{sp}^2}{\left[\frac{2P}{\dot{m}g^2} + I_{spc}^2 \right]}$$

$$P = P_{HTR} + P_D$$

$$P_{HTR} = V_{HTR} I_{HTR}$$

$$P_D = V_D I_D$$

Where: T = measured thrust, N

l_2/l_1 = moment arm ratio

Δm = chain mass increment, kg

\dot{m} = propellant flow rate, kg/s

I_{sp} = measured specific impulse, s

g = earth acceleration constant, m/s^2

I_{spc} = average cold flow specific impulse, s

P = total MEP thruster input power, W

η = measured efficiency

Note: Applied magnetic fields were provided by permanent magnets with no power consumption

Fig. 8
Equations used to Determine MEP Thruster Performance

Momentum Probe Calibration

The momentum probe system was sensitive to the flow properties of the incident plume. Specifically, in the case of free molecular flow, with the plume particles incident normal to the target, pure specular reflection will occur and the impinging particle velocity will be changed by 180 deg. with the net result being that twice the incident particle momentum will be transferred to the target. Consequently, for the pure specular reflection case, the actual thrust density will be only half the measured target thrust density. In the case of continuum flow, with the plume particles incident normal to the target, the incident particle velocity will be changed by 90 deg. and the actual thrust density will be equal to the measured thrust density. It should be noted that the momentum probe pivot (Fig. 4) orientation was such that only the thrust producing axial velocity components of the incident plume particles were sensed by the target. Defining a reflection factor, F , as a calibration multiplier for the measured momentum probe thrust density values, results in a value of $F = 1.0$ for pure continuum flow and $F = 0.5$ for free molecular flow.

In practice, the MEP thruster plume represented a transition regime which had both free molecular flow and continuum flow characteristics. The procedure used to determine the absolute accuracy of the momentum probe system involved using the apparatus to measure the cold flow specific impulse resulting from xenon expansion through a well made nozzle. Figure 9 shows a close-up photograph of the small nozzle used to perform these calibration tests. This conical nozzle had a throat diameter of 0.0406 mm, an area ratio of 1,070, and an expansion cone length of 1.27 cm. Xenon was selected as the calibrating gas since its use maximized the Reynolds number of the nozzle flow in the flow rate regime anticipated during MEP thruster testing (0 - 100 sccm).

Figure 10 shows the actual measured thrust density profiles obtained using the test nozzle shown in Fig. 9. Analysis of these profiles resulted in the xenon cold gas flow specific impulse variation shown in Fig. 11. In this figure, the Reynolds number is equal to the flow rate, in mg/s, multiplied by 140.2. It can be noted that as the Reynolds number rose to a value of 500 - 600, the measured specific impulse increased to a maximum value of approximately 44 sec. and then remained constant. This maximum nozzle efficiency behavior with increasing Reynolds number is a well known phenomenon.⁸

From Ref. 9, the maximum practical cold flow specific impulse for xenon through a well made nozzle is about 28 - 30 sec. Comparing this information with the data in Fig. 11 suggests that the momentum probe reflection factor should be of order 0.7 to calibrate the probe for this xenon flow example.

For all of the MEP thruster geometries tested during this Phase I investigation, cold flow specific impulse measurements were taken using the 33% N_2 /67% H_2 test gas mixture at various flow rate

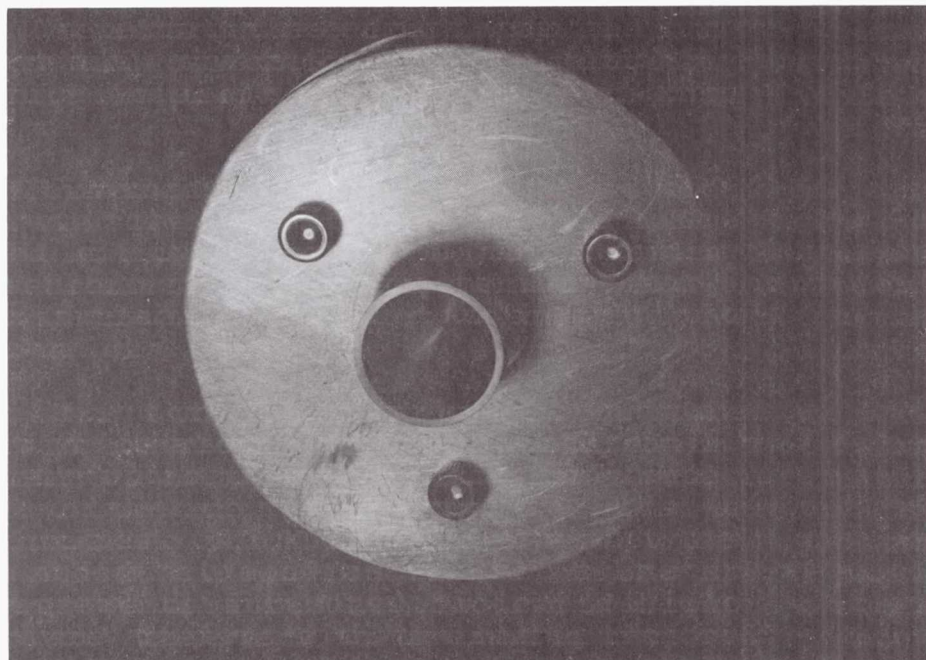


Fig. 9
Close-up Detail of Nozzle used in Xenon Cold Gas Flow Tests

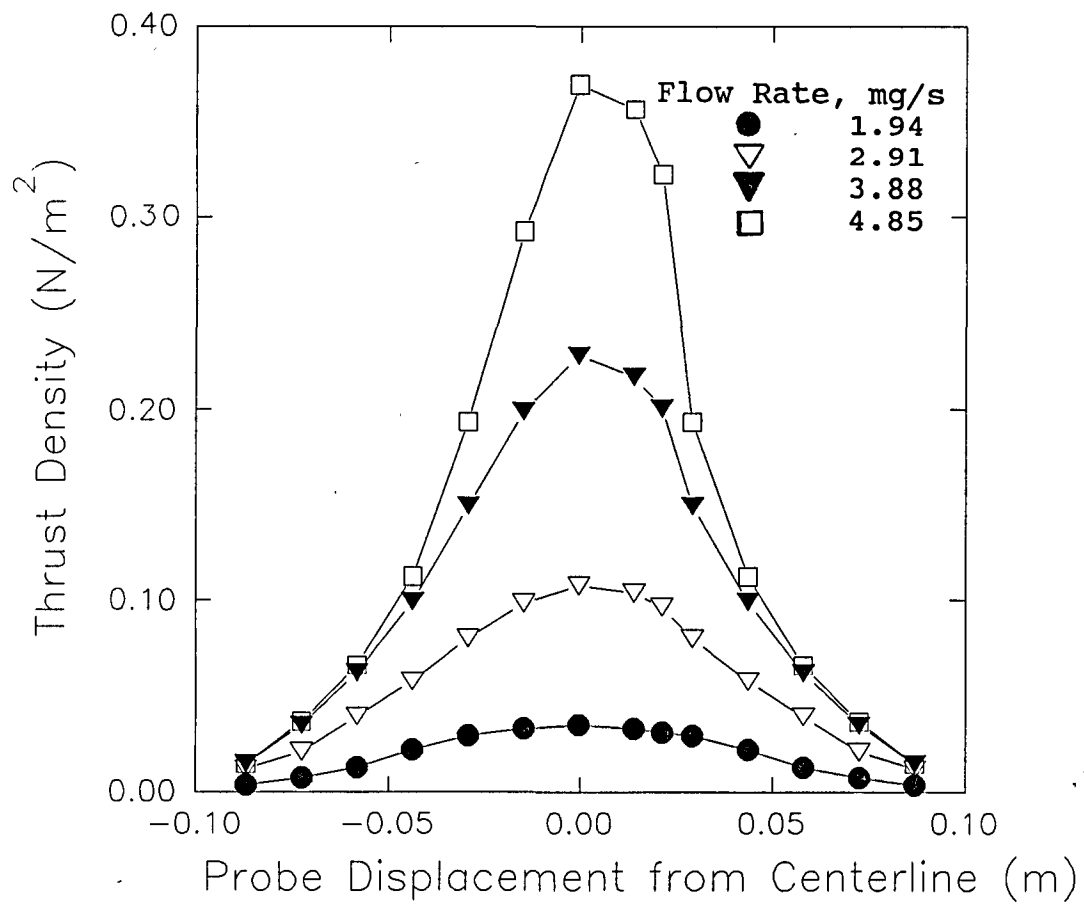


Fig. 10
Measured Thrust Density Profiles Obtained With Xenon Propellant
Assuming a Reflection Factor of 1.0

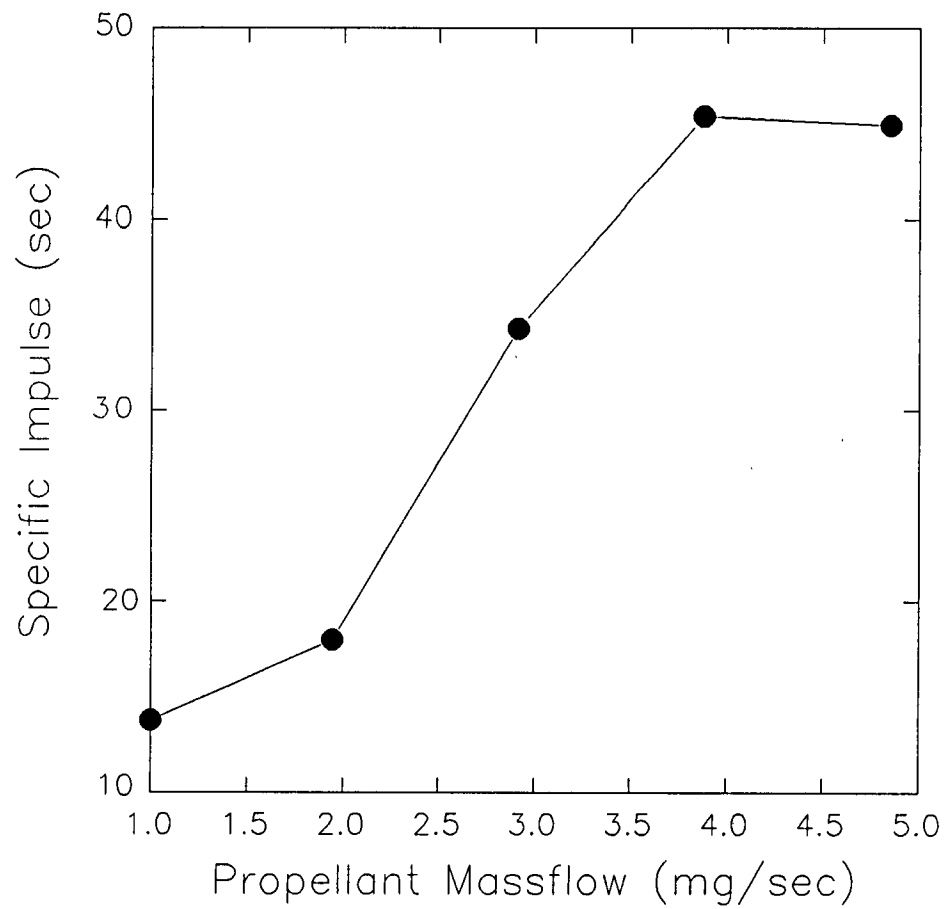


Fig. 11
Xenon Cold Gas Flow Specific Impulse Assuming a Reflection Factor
 $F = 1.0$

settings from 20 - 100 sccm. The results of these measurements indicated an average, as measured, cold flow specific impulse of 120 ± 30 sec. Reference 10 describes cold flow specific impulse measurements for a wide range of nozzle geometries using a 33% N_2 /67% H_2 gas mixture. The results presented in Ref. 10 showed a cold flow specific impulse variation of 108 ± 8 sec. for the nozzle geometries evaluated. The general similarity of the Ref. 10 nozzle geometries with the MEP thruster emitter and anode configurations tested during this present program, suggests that the momentum probe reflection factor for simulated hydrazine plumes may be as high as $F = 0.9$.

For the plume thrust density profiles presented in this report, all results are plotted with the "as measured" momentum probe system target thrust density readings. Where tables, or plots of MEP thruster performance are given, values of specific impulse, efficiency and thrust-to-power ratio are presented for reflection factors of $F = 0.75$ and 1.0 .

Error Specification

For all the data presented in this report, the following momentum probe system parameters were determined to have the uncertainties shown:

Chain, ohms/cm	± 0.5
Chain, g/cm	± 0.0002
Probe Translation, ohms/cm	± 0.2
Hair Angle, deg.	± 1.0
Target Area, cm^2	± 0.05
Moment Arm Ratio	± 0.02

The metered MEP thruster heater and anode voltages were obtained using a DVM measuring the voltage drop recorded by sense leads at the heater and anode locations and were recorded with an error of $\pm 2\%$ of the indicated reading. Similarly, the heater currents were recorded using current shunt calibrated meters and had an error of $\pm 3\%$ of the indicated reading. As described previously, mass flow calibration tests were performed using a volume bleed down apparatus which showed that the indicated mass flow controller reading was within $\pm 3\%$ of the actual MEP thruster mass flow.

The most significant error in evaluating MEP thruster performance was caused by the dangling chain length uncertainty which was ± 1.0 ohm. This error was due to the chain take-up spool potentiometer which could be read with a DVM to a resolution of only ± 1.0 ohm. For MEP thruster operation at low thrust densities, such as geometries with expanded, low density plumes, this chain length uncertainty caused increasingly large thrust density relative errors. That is, for divergent plumes, the edge thrust densities contributed significantly to the total integrated thrust, and so the net effect was a relatively large uncertainty in the total calculated thrust. However, it should be noted that this chain length uncertainty resulted in a

considerably reduced error contribution as MEP thruster operation was improved and plasma plume divergence decreased with subsequent thrust density increases.

The run-to-run repeatability of the MEP thruster performance parameters was actually quite good. Typically, for the same MEP thruster geometry, repeated data runs at identical operating conditions, resulted in specific impulse and thrust variations in the range 5 - 7%, with corresponding efficiency variations of order 15%. In addition, the merit of the momentum probing system, as it was applied to MEP thruster performance evaluation, was that it did have adequate sensitivity to differentiate between the relative performance enhancements resulting from different MEP thruster geometrical, or operating condition, changes. Finally, the capability of the momentum probing system to measure the actual plume thrust density profiles gave some insight into the potential mechanisms operating to accelerate the MEP thruster discharge plasma.

MEP ELECTRON EMITTER

The successful development of a miniature plasma accelerator requires a device which efficiently produces electrons for propellant ionization. To meet this challenge, EPL designed an advanced technology hollow cathode which featured a high degree of component integration.

Design Features

EPL has advanced hollow cathode technology by iterative cathode design improvements. In 1988, under SDIO support, EPL developed a high current (50 A class) hollow cathode using an external cartridge heater.¹¹ In 1989/90, under combined company funding and support from the Center for Advanced Space Propulsion (CASP), EPL further improved upon this high current hollow cathode design by combining the insert and orifice plate into one appropriately machined and impregnated porous tungsten billet.¹²

To effectively build upon these advancements, EPL determined that the electron emitter for the MEP thruster should have the following general characteristics:

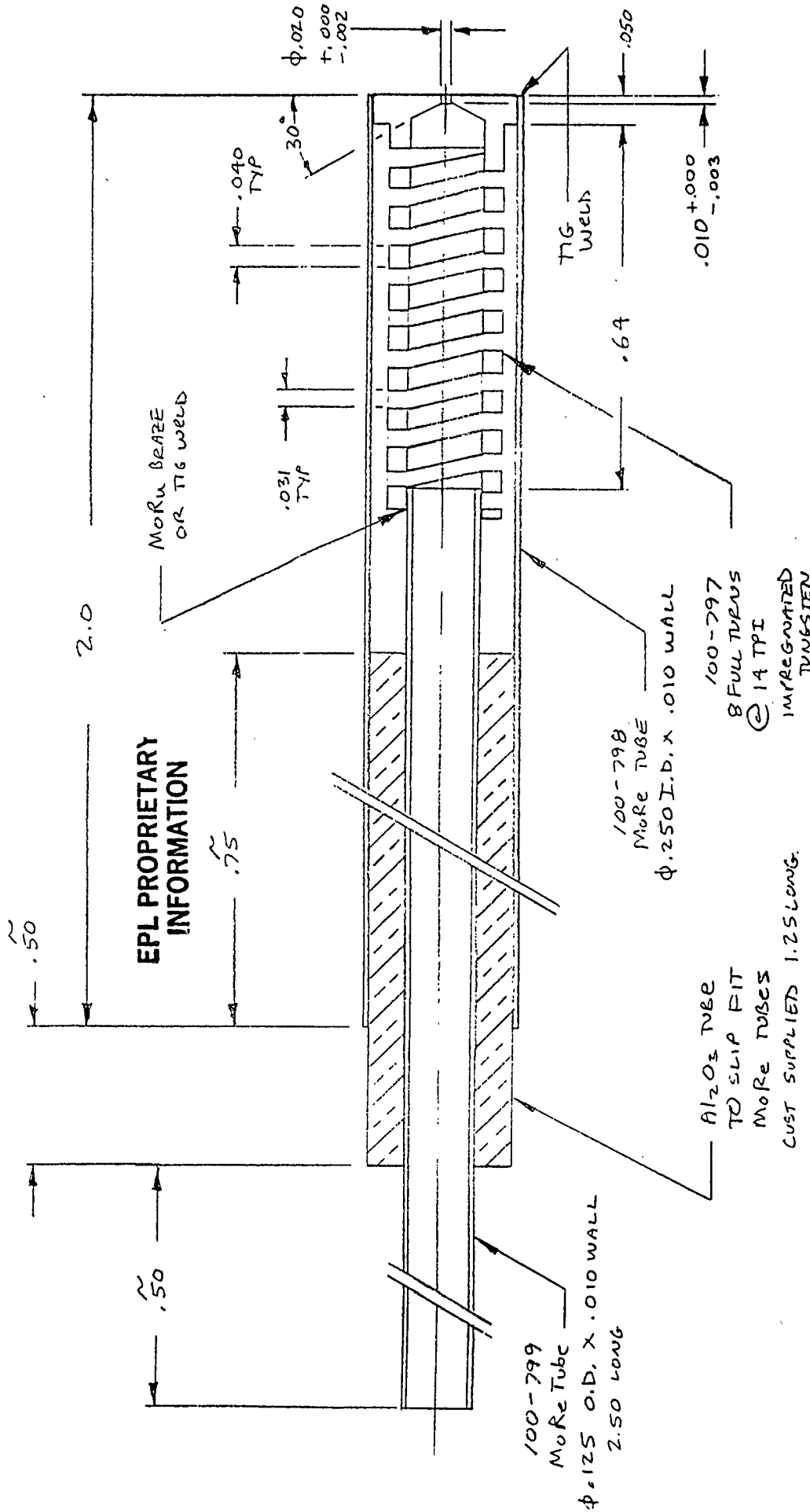
1. Low mass.
2. Small size.
3. Minimal thermal power loss.
4. Reliable arc starting characteristics.
5. Small self-heating input power requirement.

Using these self-imposed criteria as design guidelines, EPL combined the functions of the insert, orifice plate and cartridge heater into one appropriately machined and impregnated component. Figures 12a - 12d detail the design of this highly integrated hollow cathode, which was used as the electron emitter for all MEP thruster testing during this program.

Under a separate program, EPL has demonstrated hollow cathode operation on nitrogen gas for several hours duration at emission currents of 10 - 15 A.¹³ These tests were performed using a hollow cathode emissive mix which comprised a 4:1:1 molar ratio of barium oxide, calcium oxide and aluminum oxide. Based on this prior experience, EPL selected an identical emissive mix material for impregnation into the helical insert shown in Figs. 12a and 12d.

Operating Characteristics

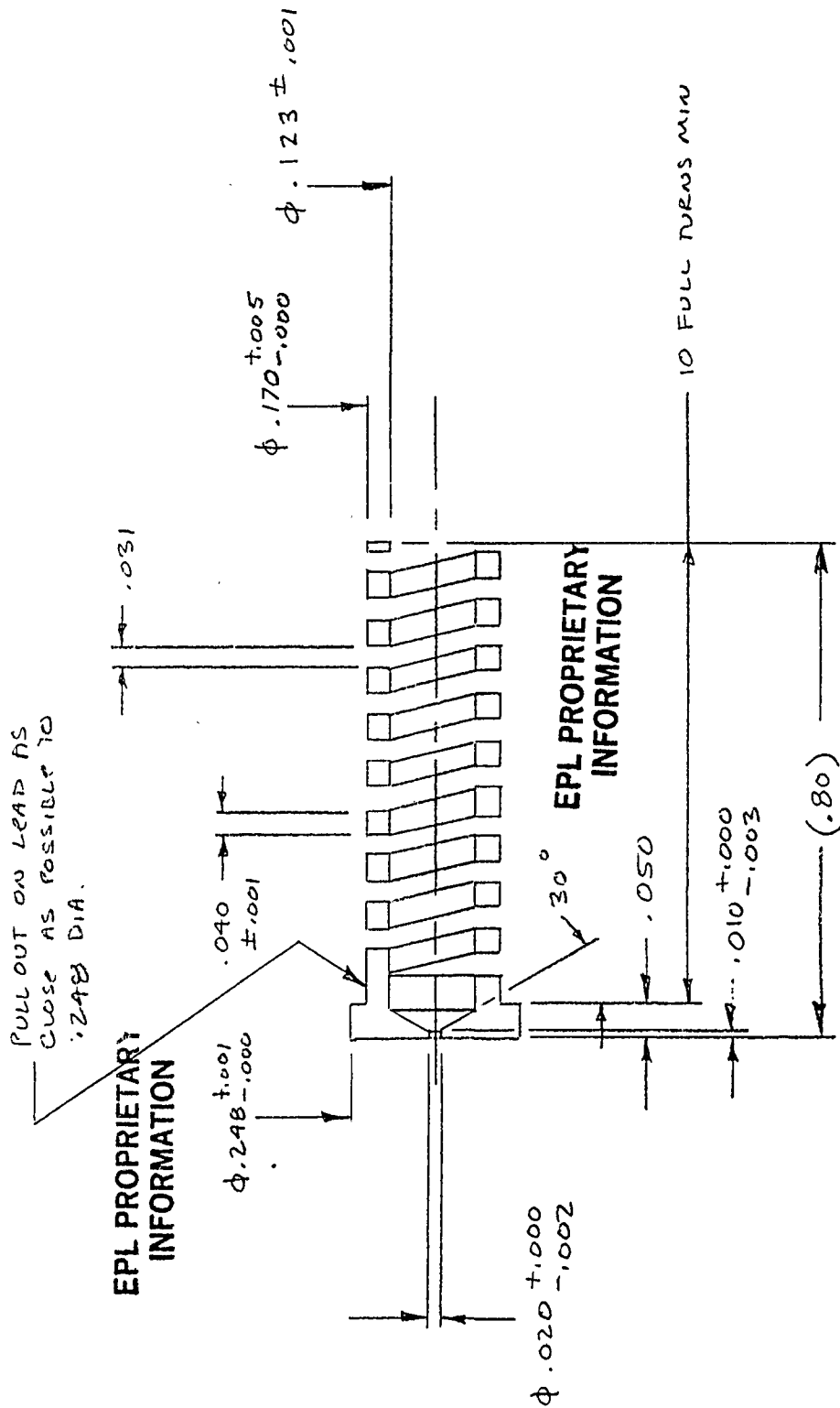
Figure 13 shows photographs of the MEP electron emitter fabricated for this program in accordance with the drawings detailed in Figs. 12a - 12b. To initiate electron emission from the hollow cathode shown in Fig. 13, a D.C. current was passed through the relatively high resistance of the helical insert (Fig. 12b). This current heated the insert to a temperature adequate for thermal electron emission after a short heating



UNLESS OTHERWISE SPECIFIED DIMENSIONS ARE IN INCHES	
.XXX +.005	.XX +.02
FINISH 63 MICROINCH	
ANGLES 8 DEG. 30 MIN	
EDGES AND CORNERS	
.005 R MAX	

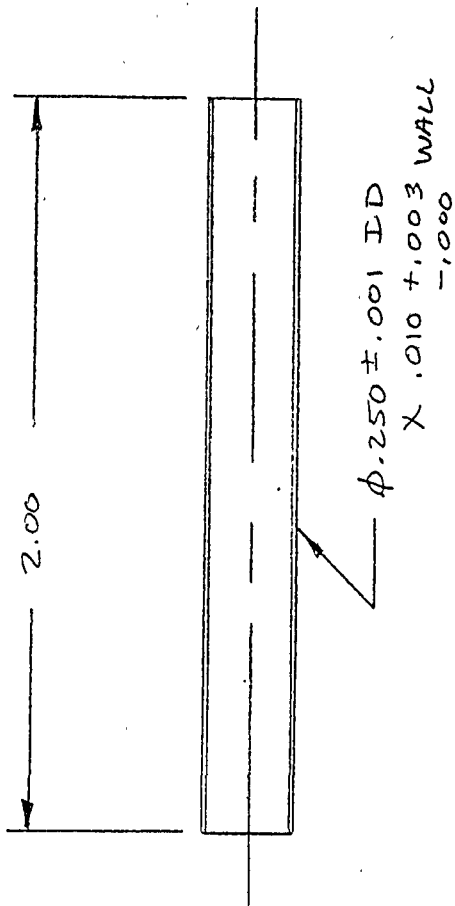
EPL PROPRIETARY
INFORMATION

Fig. 12a
MEP Electron Emitter Assembly Drawing



UNLESS OTHERWISE SPECIFIED DIMENSIONS ARE IN INCHES	
.XX ± .005	.XX ± .02
FINISH 63 MICROINCH	
ANGLES 8 DEG. 30 MIN	
EDGES AND CORNERS	
.005 R MAX	
MATERIAL	
00080 TUNGSTEN	

Fig. 12b
Detail of MEP Emitter Showing Integration of Orifice Plate,
Insert and resistance Heater into one Component

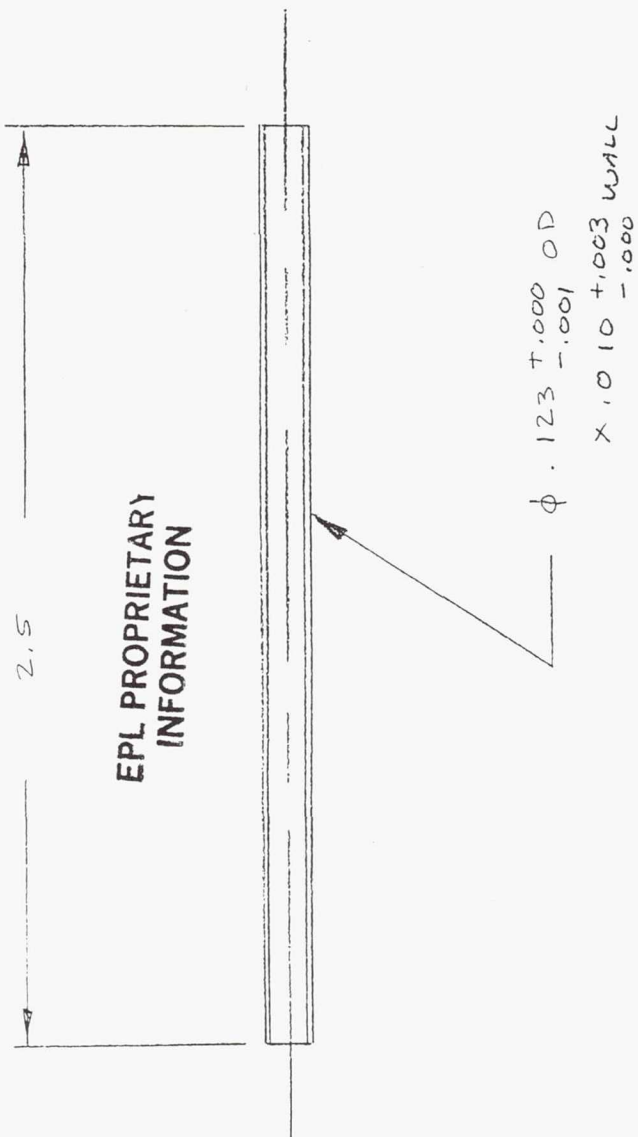


EPL PROPRIETARY
INFORMATION

EPL PROPRIETARY
INFORMATION

UNLESS OTHERWISE SPECIFIED DIMENSIONS ARE IN INCHES	
.XXX + .005	.XX + .02
FINISH 63 MICROINCH	
ANGLES 8 DEG. 30 MIN	
EDGES AND CORNERS	
.005 R MAX	
MATERIAL	
MoRe	

Fig. 12c
Emitter Hollow Cathode Outer Body Tube



EPL PROPRIETARY
INFORMATION

UNLESS OTHERWISE SPECIFIED DIMENSIONS ARE IN INCHES	
.XXX +.005	.XX +.02
FINISH 63 MICROINCH	
ANGLES 8 DEG. 30 MIN	
EDGES AND CORNERS	
.005 R MAX	
MATERIAL	
MoRe	

Fig. 12d
Emitter Hollow Cathode Inner Body Tube

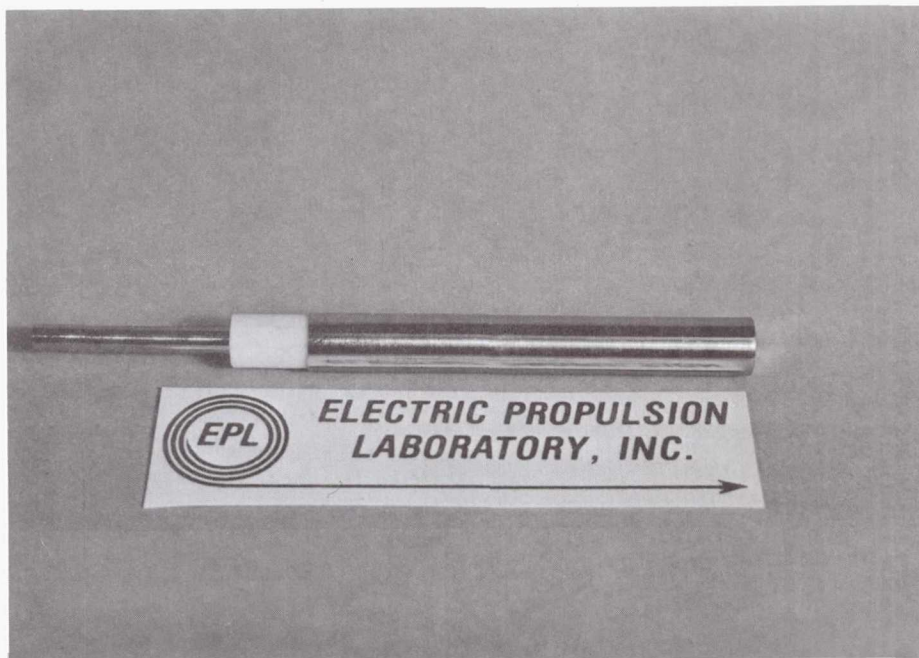


Fig. 13a
MEP Electron Emitter

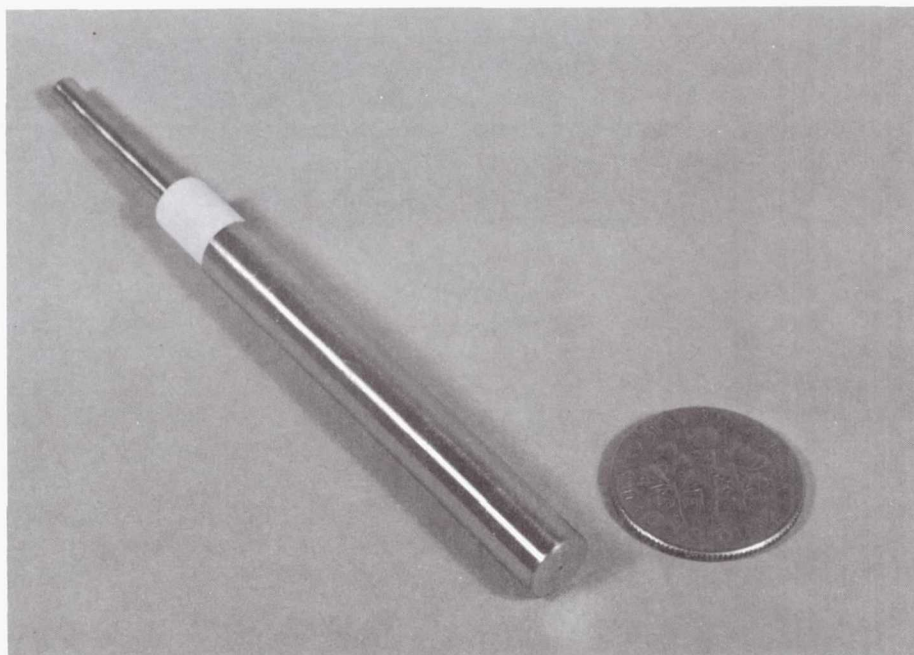


Fig. 13b
MEP Emitter Showing Orifice with Dime for Size Comparison

period of 1 - 2 min. Note in Fig. 12a and Fig. 1, that the circuit for this heating current was through the outer MoRe cathode body tube, through the helical insert, and through the MoRe inner cathode body tube.

The MEP electron emitter heater current and voltage characteristics varied with the particular MEP thruster geometry under test, and the thermal losses attendant to that test geometry. Due to the contract requirement for modular MEP thruster test geometries, to allow for complete component disassembly and inspection after testing, the thermal environment around the emitter had a higher loss rate than if the separate MEP thruster components had been integrated into one assembly. Figure 14 shows a plot of the emitter heater voltage variation, for a fixed heater current, for a typical MEP thruster test configuration. As noted in this figure, propellant flow through the emitter had the effect of cooling the helical insert, thus lowering its resistance and the subsequent heating current voltage drop. This behavior of the helical insert is similar to that of a resistojet.

During this program, the cumulative MEP emitter heater on-time was 25.1 Hrs. Approximately one hundred and fifty MEP thruster discharge starts were accumulated throughout this Phase I investigation. During the first few times the emitter heater was turned on, the heating current was gradually raised from an initial value of about 9 A to a final value of about 16 A over a period of several minutes. However, as confidence was gained in the emitter operating characteristics and in the robustness of the device, this procedure was eliminated and the full 16 A heating current was applied immediately when the emitter was turned on.

As noted in Fig. 1, the hollow cathode discharge was initiated between the emitter and a downstream anode. For most of the tested geometries, the emitter hollow cathode discharge was initiated by applying a few tens of volts to the downstream anode(s), and either pulsing the propellant flow, or establishing a minimum gas flow rate. Similarly, after start-up, most test geometries permitted stable emitter operation with no applied heater power. This easy starting behavior, and ready self-heating characteristic, was directly attributable to the helical insert design incorporated into the emitter. Specifically, direct resistance heating of the insert permitted high starting temperatures to be attained quickly, subsequently yielding a large production of thermal electrons. Furthermore, once a low breakdown voltage arc discharge had been established, the relatively low thermal mass and low thermal conduction heat loss of the helical insert, allowed the insert to self-heat with a relatively small discharge current.

Propellant Compatibility Testing

An important requirement in proof-of-concept testing of the MEP thruster was that the emitter hollow cathode insert

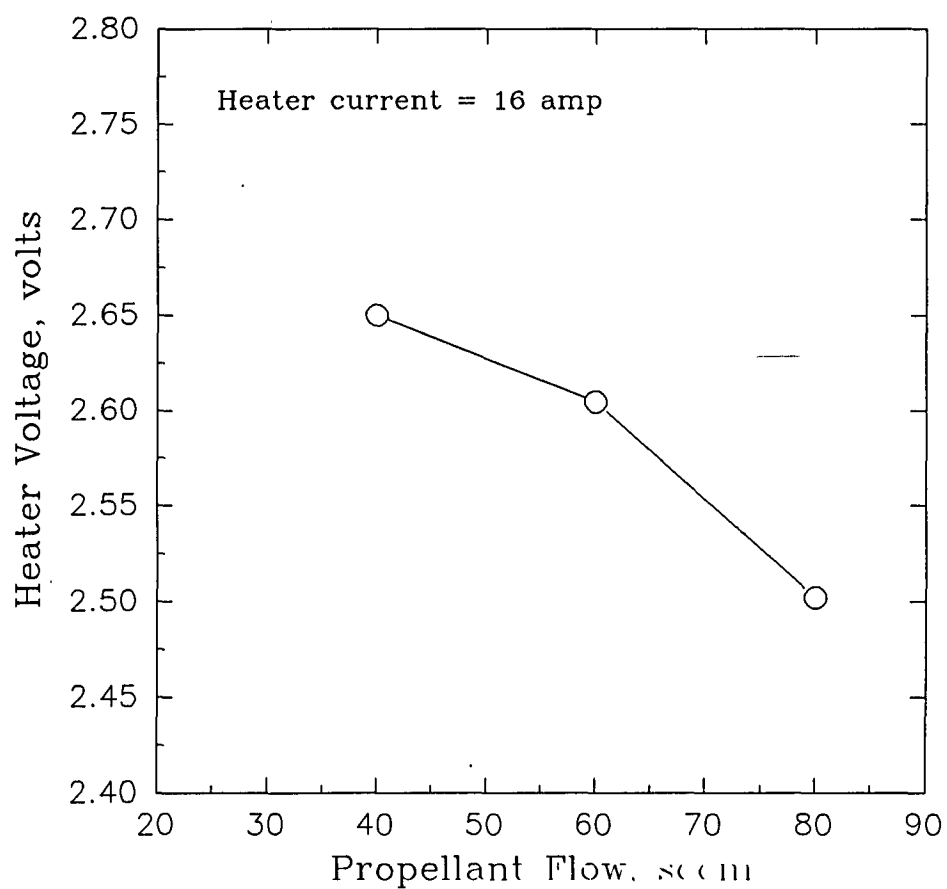


Fig. 14
Typical Reduction in Helical Insert/Heater Voltage, at Constant
Current, for MEP Emitter Due to Heat Transfer to Flowing
Propellant

impregnant be compatible with decomposed hydrazine. In order to verify this compatibility, the MEP emitter was operated on 33% N_2 \ 67% H_2 in a simple diode configuration (Fig. 1). Figures 15 and 16 document the assembly of the MEP emitter and test anode for these tests. The anode was a simple flat molybdenum plate of thickness 0.381 mm, with a hole diameter of 1.70 mm, which was positioned 0.64 mm downstream of the emitter exit plane (ie. the downstream face of the orifice plate).

The MEP emitter was operated for a continuous period of five hours during these propellant compatibility tests. The first four hours were at an anode current of 2.0 A (the contract specification), while the last hour was used to investigate behavior at a variety of mass flow rates and emission currents up to 4.0 A. Figure 17a shows the emitter operating at 2.0 A during the four hour test period, and Fig. 17b shows operation at 4.0 A during the one hour of parametric testing. Table 1 summarizes the MEP emitter operating characteristics during the five hour test period. As is evident from these data, the MEP emitter heater plasma discharge current and voltage characteristics were essentially unchanged during the four hour test period, thus verifying compatibility with decomposed hydrazine. It is important to note that the MEP emitter discharge was initiated at an open circuit anode bias voltage of 40 V following passage of a starting gas pulse through the emitter orifice. Furthermore, the data in Table 1 show emitter operation from time zero which corresponded to "as received condition" from the fabrication vendor. EPL performed no insert thermal cycling, or otherwise preconditioned the insert, prior to the start of these tests.

During the one hour of parametric testing documented in Table 1, MEP emitter operation was explored up to a maximum total heater and discharge power of 153 W. Figures 18a and 18b show before and after details of the emitter orifice and tip region before and after this five hour test program. The photographs in these figures show no evidence of damage or erosion resulting from five hours of continuous operation at up to this 153 W total input power level.

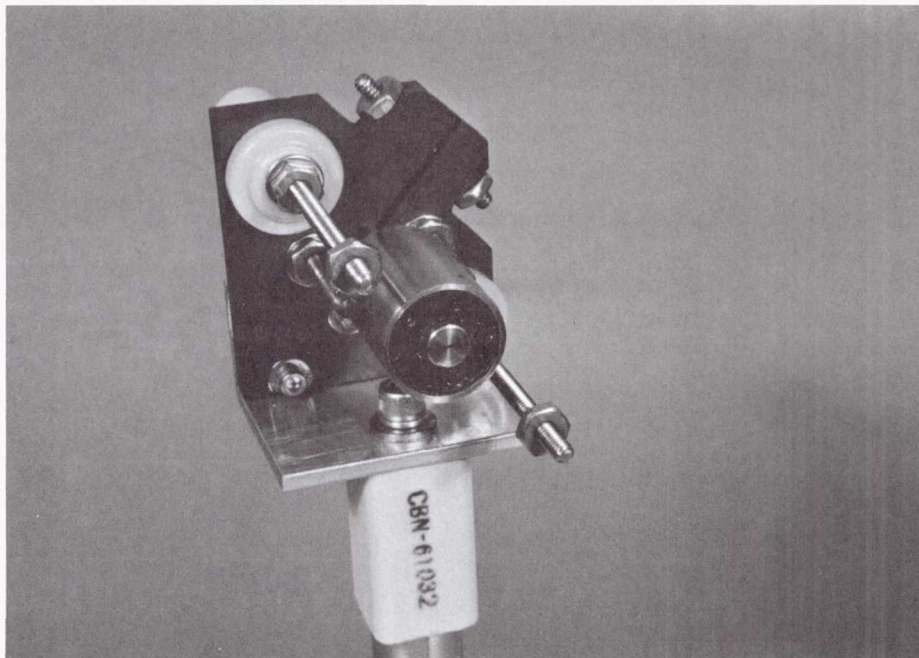


Fig. 15a
MEP Emitter in Test Fixture Showing Multiple Wrap Tantalum
Radiation Shielding to Limit Radial Heat Loss

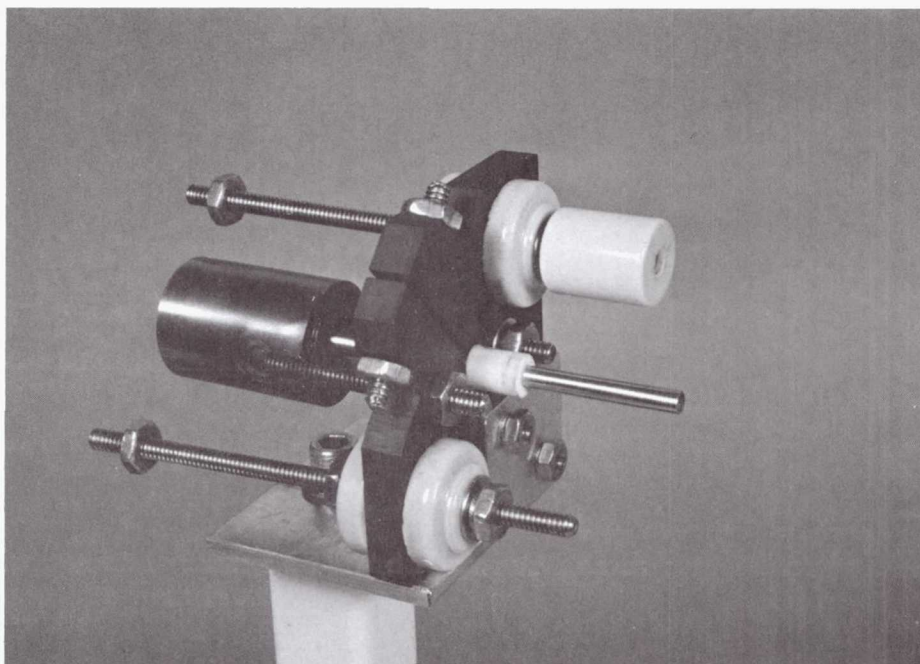


Fig. 15b
Test Fixture Detail Showing Graphite Block Clamping Arrangement
on Emitter Tube

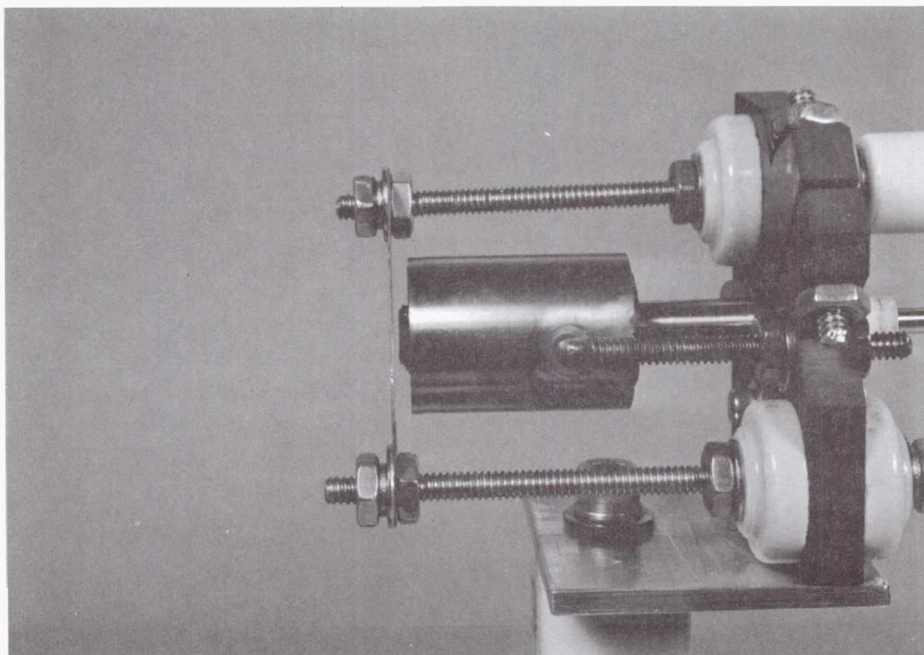


Fig. 16a
Emitter with Simple Flat Plate Anode

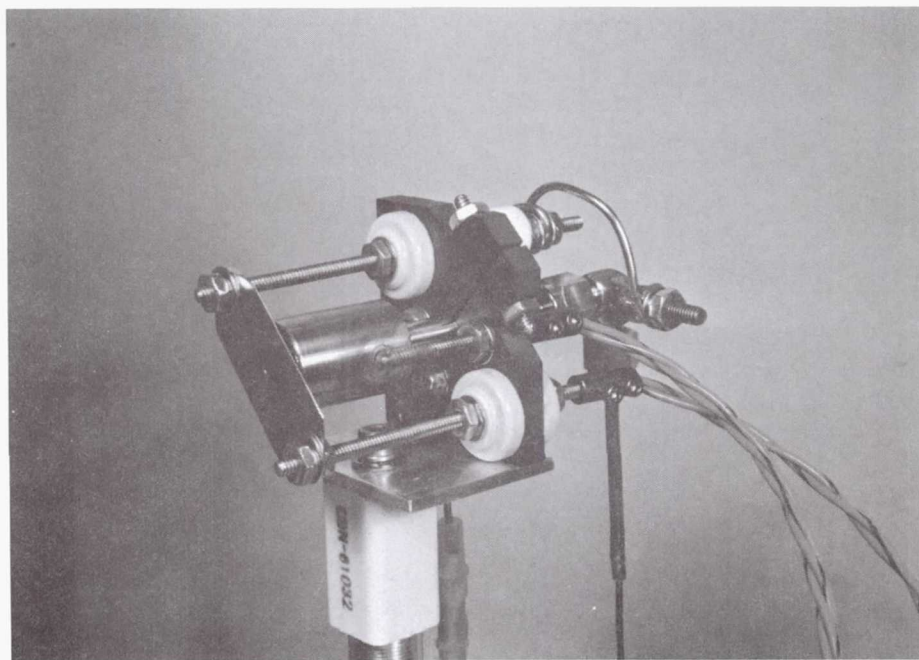


Fig. 16b
Final Assembly of MEP Emitter, in Diode Configuration, Showing
Power Leads and Propellant Line



Fig. 17a

MEP Emitter During Four Hour Propellant Compatibility Test at
Constant 2.0 A Anode Current with Average Input Power of
Approximately 72 W



Fig. 17b

MEP Emitter Operating at 4.0 A Anode Current at an Average Input
Power of 153 W

Table 1. MEP Emitter Performance Characteristics During Five Hour Propellant Compatibility Test Sequence

Time min.	Flow sccm	V _{HTR} volts	I _{HTR} ampere	V _D volts	I _D ampere
3	55	2.01	15.0	21.9	2.00
10	55	2.00	15.0	21.2	2.00
20	55	1.99	15.0	20.9	2.00
31	55	1.99	15.0	20.8	2.00
46	55	1.98	15.0	20.6	2.00
63	55	2.04	15.5	20.2	2.00
132	54.9	2.03	15.2	20.5	2.00
163	55	2.00	15.0	20.7	2.00
223	55	2.01	15.0	20.5	2.00
240	55	2.02	15.0	20.4	2.00
245	65	2.00	15.0	20.4	2.00
250	45	2.01	15.0	20.9	2.00
255	40	2.01	15.0	20.9	2.00
260	36	2.02	15.0	21.8	2.00
265	33.5	2.04	15.0	23.1	2.00
270	42.8	2.05	15.0	20.0	3.00
275	44.6	2.08	15.0	18.7	4.00
280	44.6	1.86	14.0	23.5	4.00
285	44.6	1.71	13.0	28.2	4.00
290	44.6	1.46	11.5	34.0	4.00
296	Operator shutdown.				

Note: 1 sccm 33% N₂\67% H₂ = 0.0079 mg/sec.

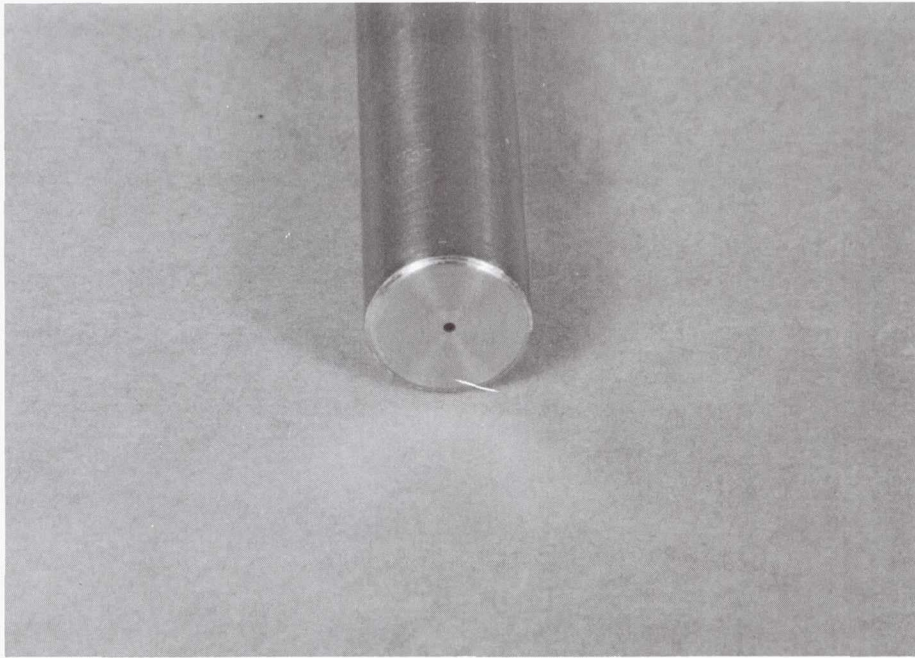


Fig. 18a
MEP Emitter Tip and Orifice Prior to Testing

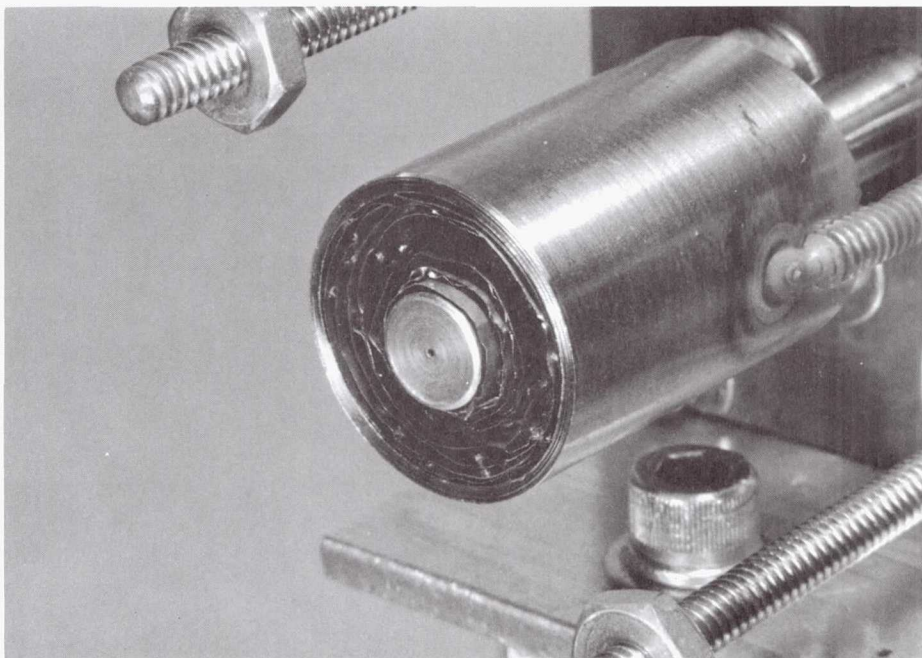


Fig. 18b
Emitter Tip and Orifice After Five Hour Test Sequence, Showing no Erosion or Damage

MEP THRUSTER PARAMETRIC TESTING

EPL used the hollow cathode electron emitter, and various anode test configurations, to investigate the feasibility of achieving useful plasma acceleration at input powers of a few tens of watts. These tests were separated into configurations identified by the general nature of the type of anode structure investigated. For most test configurations, an external magnetic field was applied. As these different anodes and magnetic fields were experimentally examined and analyzed, the dominant physical processes became evident. Eventually, a new plasma acceleration process was discovered which appeared capable of producing useful thrust at unprecedented power levels of less than 50 W. The following sections give an approximate chronological summary of these tests.

Plate Anodes

After successfully completing the emitter propellant compatibility tests which involved a single plate anode, various tests were performed using different plate anode geometries. These tests were useful in gaining further experience in the MEP thruster start-up and operating characteristics, and culminated in testing of a triple plate anode structure shown in Figs. 19a - 19d. As noted in Fig. 19a, the three molybdenum plate anodes had hole diameters which increased with increasing separation from the emitter exit plane. Each anode was 0.38 mm thick, and the hole diameters were 1.6 mm, 3.2 mm and 6.4 mm. The separation of the closest (ie. smallest hole diameter) anode from the emitter exit plane was 0.64 mm, while the anodes themselves were separated by gaps of 0.76 mm.

Separate current meters were used to monitor the discharge current going to each of the anodes identified in Fig. 19a. In addition, each anode could be switched out of the circuit for floating potential measurements. The results of these tests revealed that virtually all of the discharge current went to the farthest downstream anode, regardless of operating conditions. Similarly, it was noted that all anodes floated at essentially the downstream anode potential.

Table 2 summarizes the results of tests performed with the triple thin plate anode MEP thruster configuration. Although as evidenced by Fig. 19d, a bright expanding plume emanated from the MEP thruster when a plasma discharge was established, thrust density measurements showed negligible gas acceleration was occurring as a result of this discharge; the plume shown in Fig. 19d corresponded to a discharge current of 0.6 A, a discharge voltage of 42 V, and a heater power of 41 W. Typically, specific impulse measurements indicated virtually identical values with the insert heater on, and with the heater on and a plasma discharge established.

The principle benefit noticed with the multiple thin anode plates downstream of the MEP emitter was that the anode plates

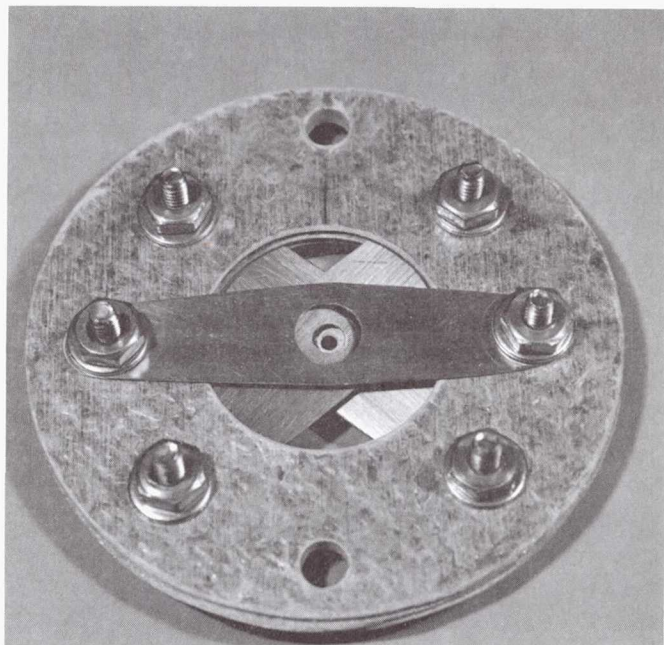


Fig. 19a
Triple Thin Plate
Anode Structure

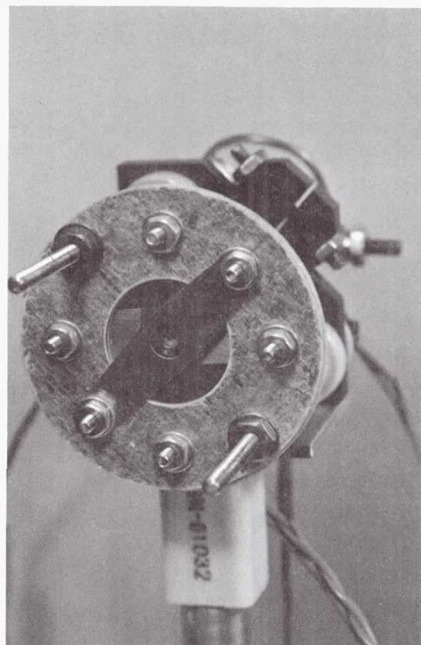


Fig. 19b
MEP Thruster Configured
with Three Isolated Anodes

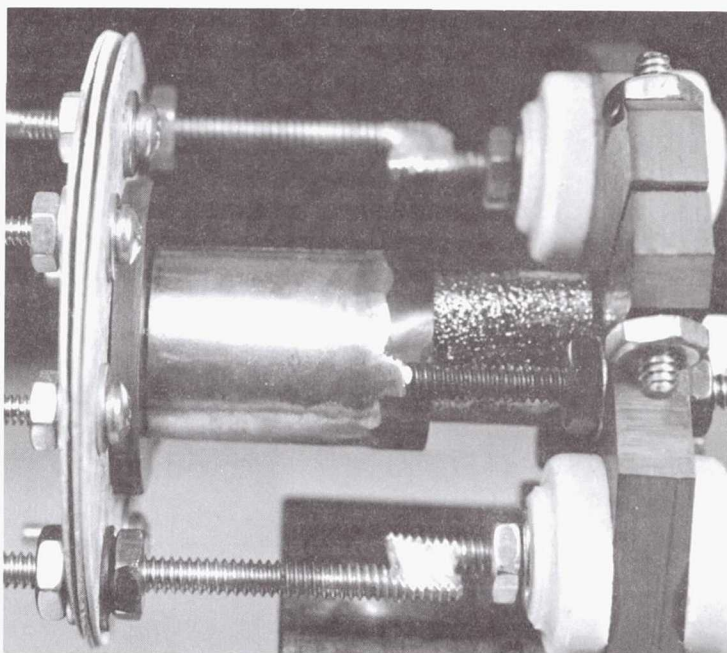


Fig. 19c
Side View of MEP Thruster
Configuration Shown in Fig. 19b

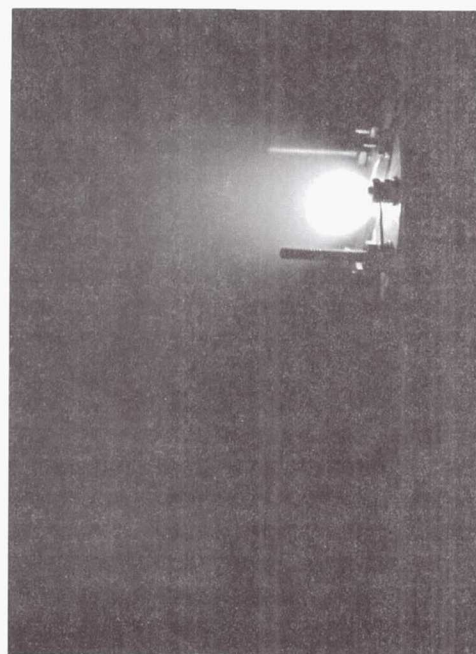


Fig. 19d
Plume Typical of Triple
Plate Anode MEP Thruster
Discharge

Table 2. MEP Thruster Performance Using a Triple Plate Anode Configuration and Assuming a Reflection Factor of $F = 1.0$

Flow	P_{HTR}	T	I_{sp}	Eff
sccm	W	mN	s	%
20	-0-	0.15	98	N/A
100	-0-	0.72	93	N/A
20	42	0.15	96	0.16
100	40	1.31	170	2.7

Note: Zero heater power flow tests correspond to cold gas flow specific impulse measurements.

acted as radiation shields, reducing axial emitter heat loss. The net result of this better heat retention, was that the emitter insert heater acted as a resistojet, expelling hot propellant through the "nozzle" comprised of the anode plates. Specifically, electrical forces appeared to have little direct effect on the propellant acceleration. Table 2 shows that this resistojet-like behavior of the MEP thruster produced measured specific impulse values nearly twice that of the cold gas flow measurements. Similarly, these data show that this resistojet-like action of the MEP emitter was significantly more efficient at the highest propellant flow rate tested. This latter effect is typical of resistojets which generally require relatively high internal pressures to maximize heat transfer to the propellant.¹⁴

Cavity Anodes

Following the triple thin plate anode tests, an applied magnet field capability was added to the MEP thruster. Initially tests were performed using an electromagnet solenoid which is shown in Fig. 20. This solenoid was capable of generating an axial field strength of 350 - 400 Gauss in the vicinity of the MEP emitter orifice using a solenoid current of 30 A. MEP thruster operation at a discharge current of 2.0 A was investigated briefly with this solenoid, during which time the thruster plume diffuse red/yellow color was observed to change to an intense purple/white color. Shortly after this observation, the solenoid windings overheated and shorted to the solenoid coil form.

In consideration of the high temperature MEP thruster operating environment, and because it was expedient to provide a way to easily vary the applied magnetic field distribution, ring permanent magnets were substituted for the magnet solenoid. Alnico 5 material was selected for these initial ring permanent magnet tests because of its relatively high Curie temperature of 850 C.¹⁵

Figures 21a and 21b show the MEP thruster configured for testing with a ring permanent magnet. Figure 21a shows the magnet placement relative to the emitter and Fig. 21b details the anode placement. The magnet could be moved axially, relative to the emitter, to vary the magnetic field strength and direction in the region of the emitter orifice. Figure 22 plots the measured axial magnetic field strength variation for the ring magnet geometry shown in Figs. 21a and 21b as a function of pole face displacement from the emitter exit plane. As noted in Fig. 22, the ring magnet was magnetized in the axial direction to produce a predominately axial magnetic field distribution within the magnet body, and a strong radially divergent field distribution in the region of the magnet pole face (ie., $X = 0$).

A cavity anode geometry, shown in Fig. 21b, was used with the initial ring magnet MEP thruster configuration. This anode geometry was selected because it allowed for some axial ring magnet movement and also because it represented a configuration

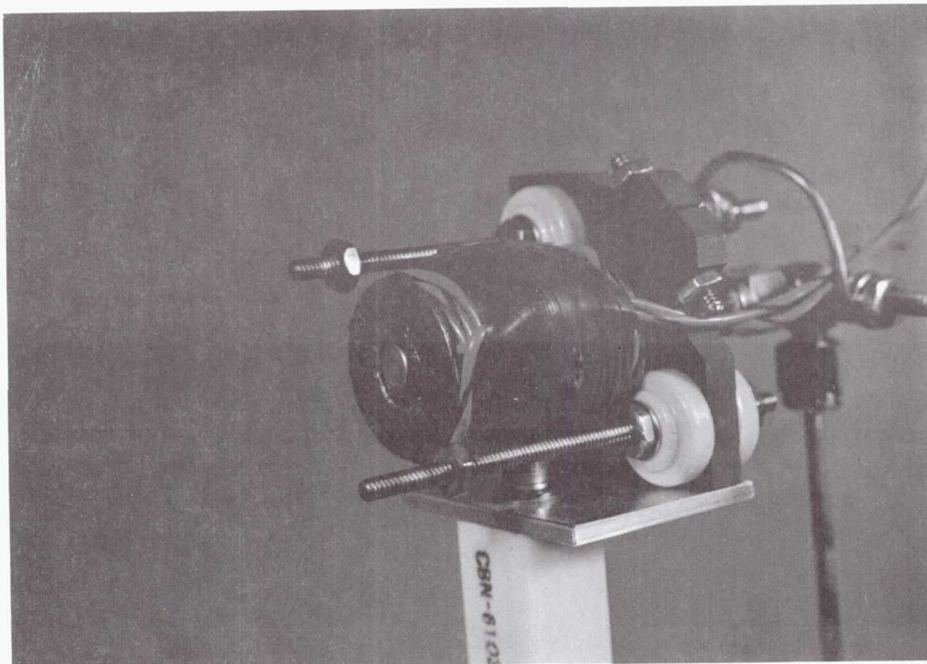


Fig. 20
MEP Thruster with Magnet Solenoid

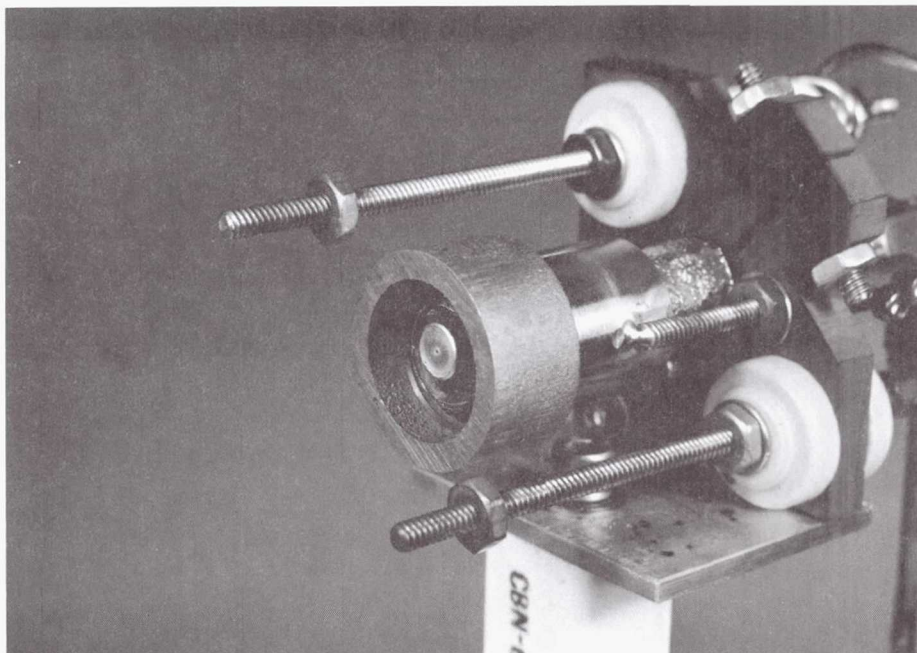


Fig. 21a
Initial Ring Permanent Magnet Geometry Positioned over MEP
Emitter

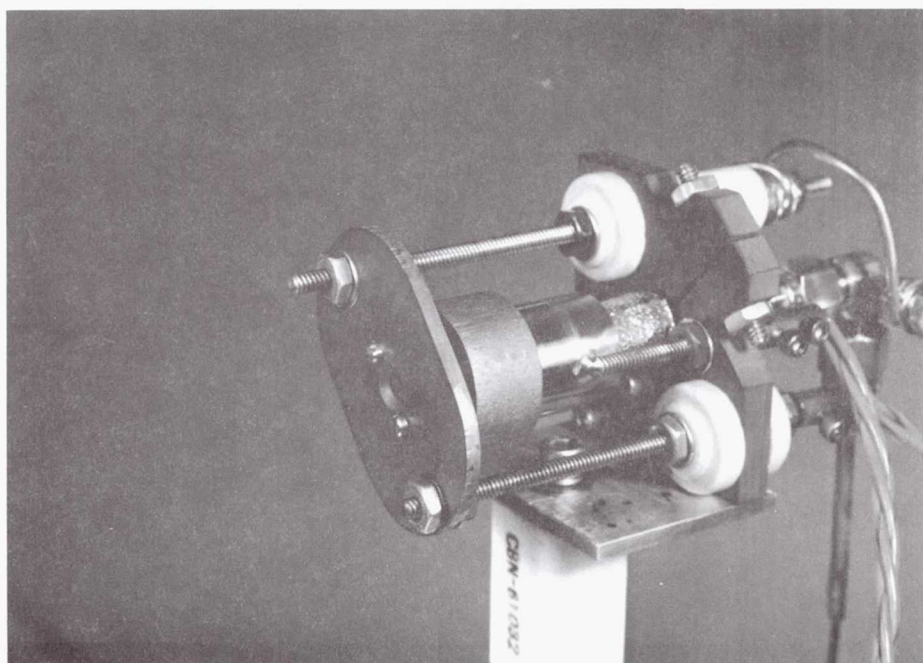


Fig. 21b
Graphite Cavity Anode Positioned in Front of MEP Thruster Emitter

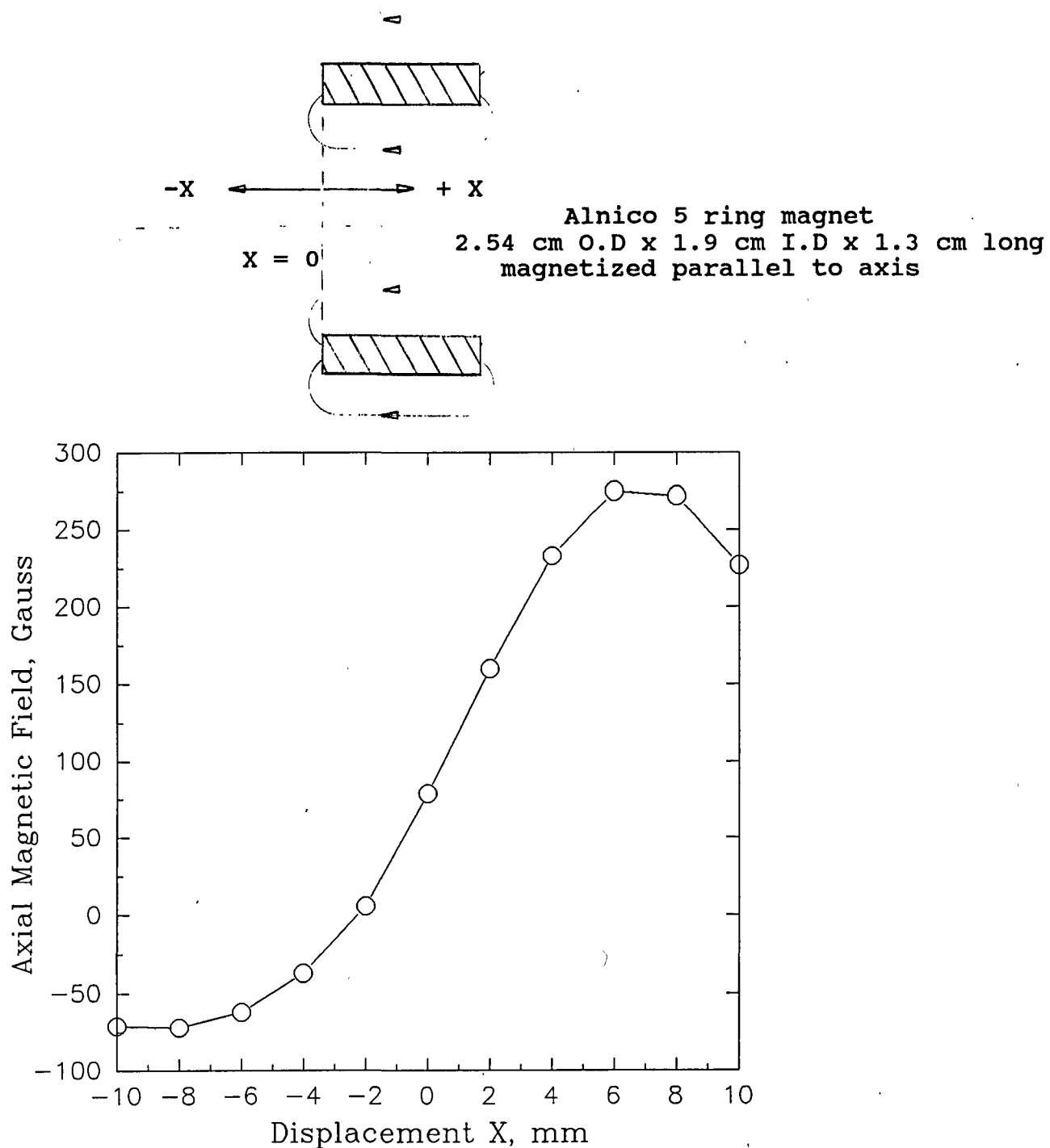


Fig. 22
Measured Axial Magnetic Field distribution for Alnico 5 Ring Magnet Shown in Fig. 21a

which increased the neutral particle pressure immediately downstream of the emitter orifice. Several cavity anode geometries were investigated during these initial applied magnetic field tests. These geometry changes primarily involved changes to the anode hole entrance diameter, and exit hole diameter and chamfer angles, to permit stable MEP thruster operation without extraneous arcing. Figure 23 details the final cavity anode design configuration for which most of the MEP thruster testing was performed.

Figure 24 documents the measured cavity anode and voltage characteristics for three different propellant flow rates. For these data, the magnet ring downstream pole face was set at $X = 2.7$ mm (as defined in Fig. 22) from the exit plane of the MEP emitter. The MEP insert heater was left on during collection of the data shown in Fig. 24 and the heater input power varied from 42 W, at a flow of 15.5 sccm, to 46 W at a flow of 2.0 sccm. The data in Fig. 24 illustrate that the MEP emitter was capable of operating at a discharge current as high as 7.0 A, and a total thruster input power as high as 219 W.

The most remarkable result of MEP thruster operation with the geometrical configuration shown in Fig. 21b and Fig. 23, was the emergence of a well defined plasma jet as the propellant flow rate was reduced. Figures 25a, 25b and 25c document the formation of this plasma jet. Similarly, Fig. 26 shows the resultant thrust density profiles recorded for these different MEP thruster operating conditions. The vacuum facility background pressures during these tests varied from 1.7×10^{-5} Torr for a flow rate of 15.5 sccm, to 9.5×10^{-6} Torr for a flow rate of 2.0 sccm.

Figures 27a - 27c plot the MEP thruster performance parameters, as a function of total thruster input power, corresponding to the thrust density profiles shown in Fig. 26. Although the measured specific impulse was very high at the lower flow rates, the overall MEP thruster efficiencies were very low. Nevertheless, these data were significant because they indicated the presence of a relatively high energy plasma jet, the formation of which apparently required a high emission current-to-propellant flow rate ratio in the presence of a diverging magnetic field.

After completion of the test sequence documented in Figs. 24 - 27, the ring magnet was removed and found to have undergone a field strength reduction of approximately 50%. This magnetic field reduction was a result of the magnet operating at near its Curie temperature, which in turn occurred because of the relatively poor thermal isolation between the magnet and hot discharge. Additional testing was performed with a new, and identical ring magnet, which was located at a position $X = 5.4$ mm (as defined in Fig. 22) from the exit plane of the MEP emitter. Corresponding specific impulse and efficiency measurements revealed considerably poorer MEP thruster performance than the performance documented in Figs. 24 - 27, where the magnet position corresponded to $X = 2.7$ mm. These results established

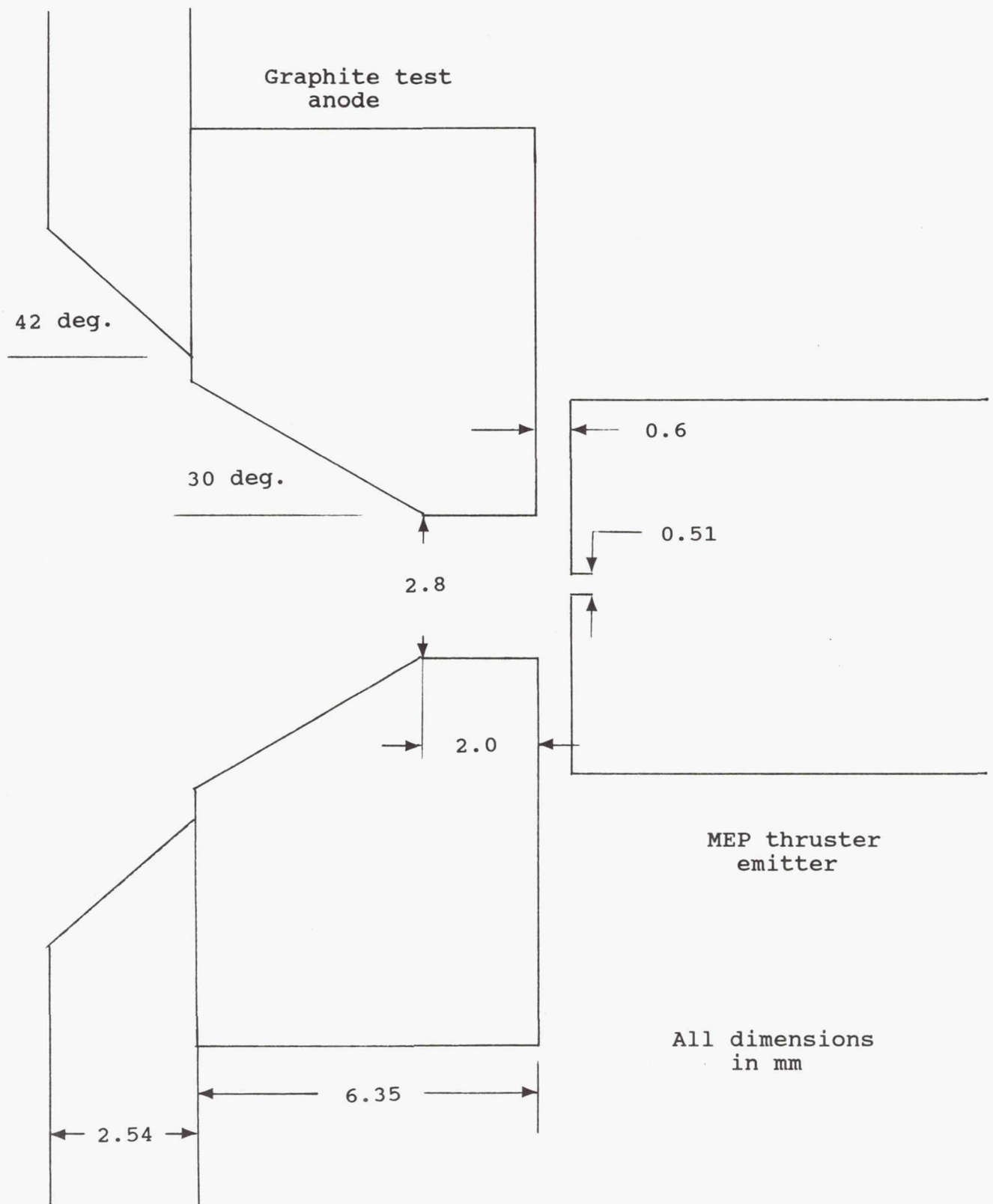


Fig. 23
Design Details of Cavity Anode Geometry used for Most of the
Initial Ring Magnet MEP Thruster Performance Tests

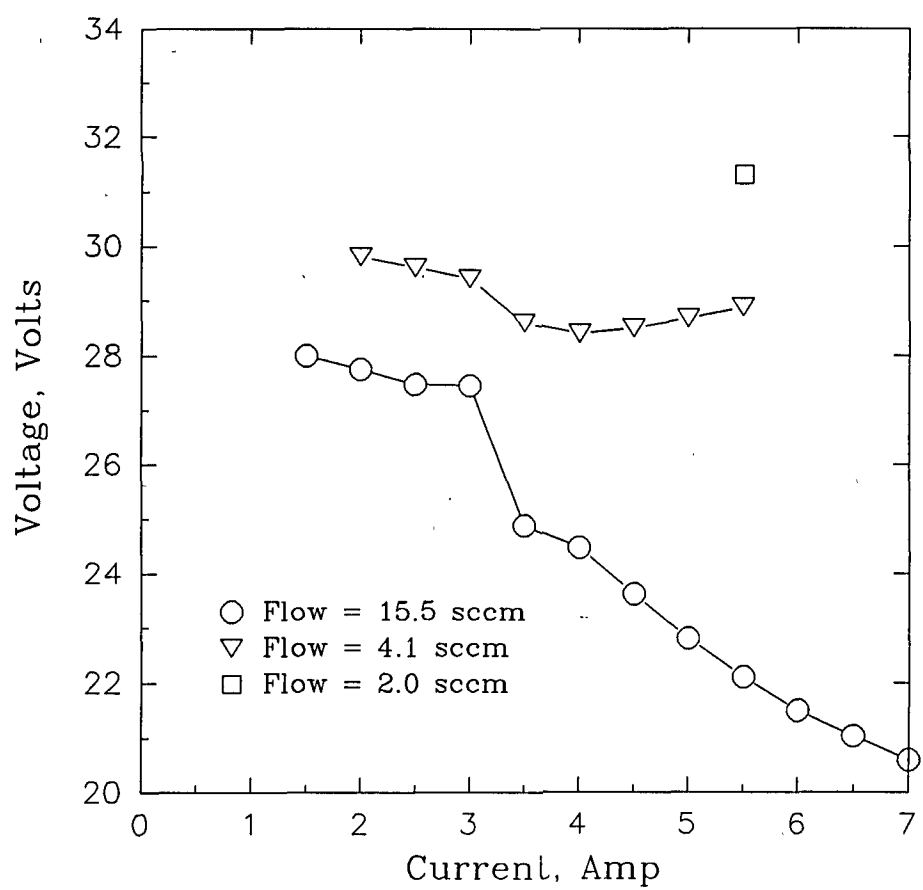


Fig. 24
MEP Thruster V-I Characteristics with Cavity Anode



Fig. 25a
Relatively Diffuse Plume Corresponding to an Anode Current of 7.0
A and a Flow rate of 15.5 sccm



Fig. 25b
Plasma Jet Starting to Emerge at an Anode Current of 5.5 A and a
Flow Rate of 4.1 sccm



Fig. 25c
Well Defined Plasma Jet Corresponding to an Anode Current of 5.5
A and a Flow rate of 2.0 sccm

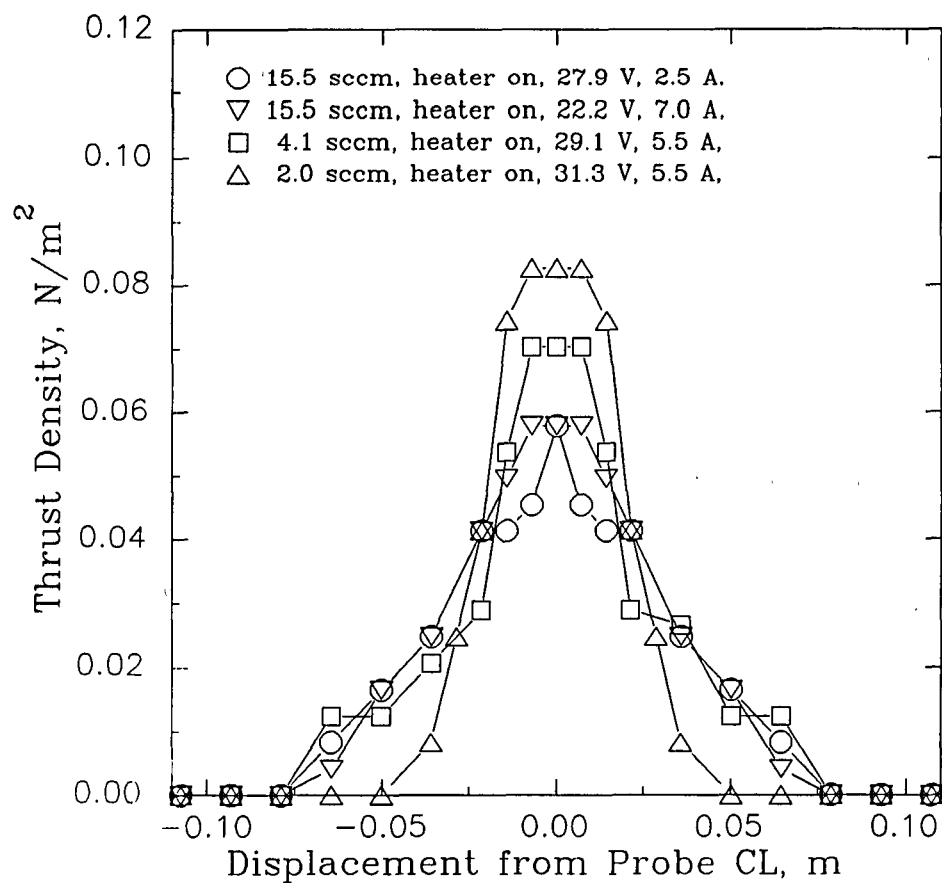


Fig. 26
Emergence of Plasma Jet Verified by Momentum Probe Plume Thrust Density Measurements

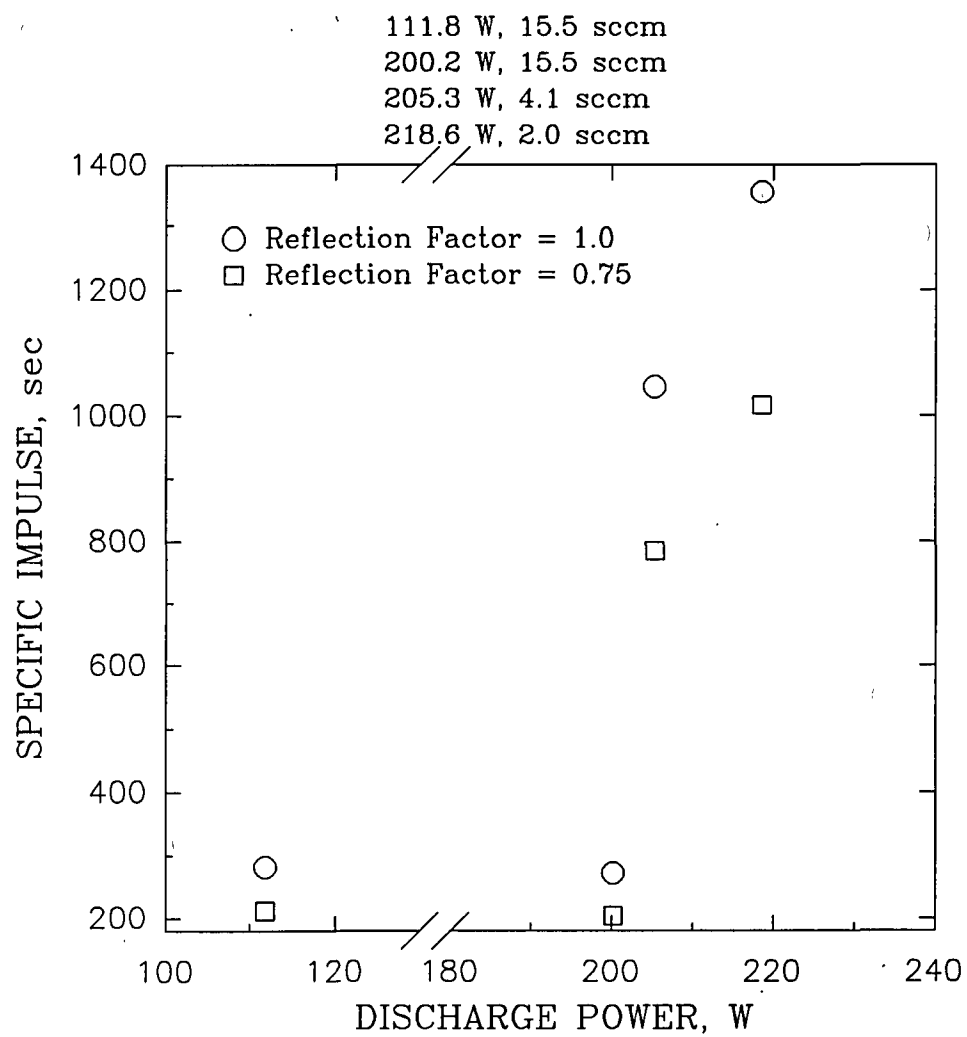


Fig. 27a
MEP Thruster Specific Impulse Characteristics with Cavity Anode

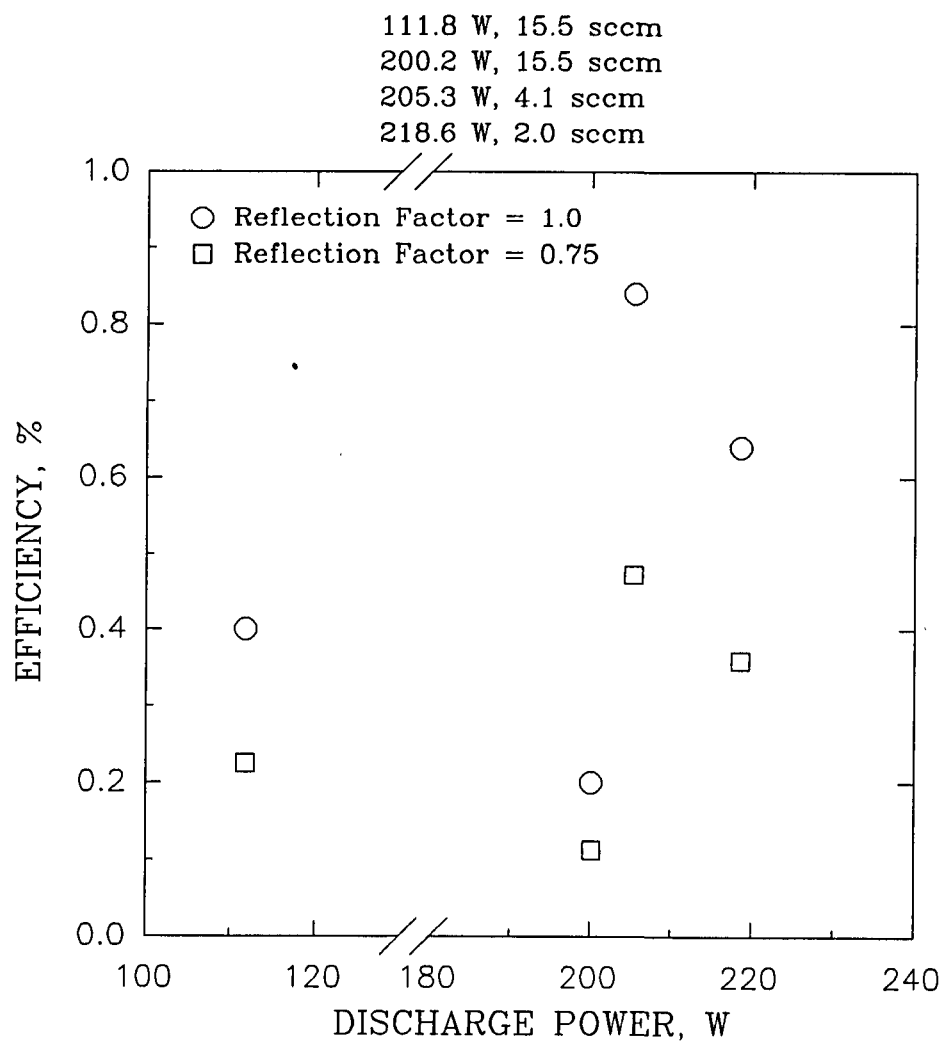


Fig. 27b
MEP Thruster Efficiency Characteristics with Cavity Anode

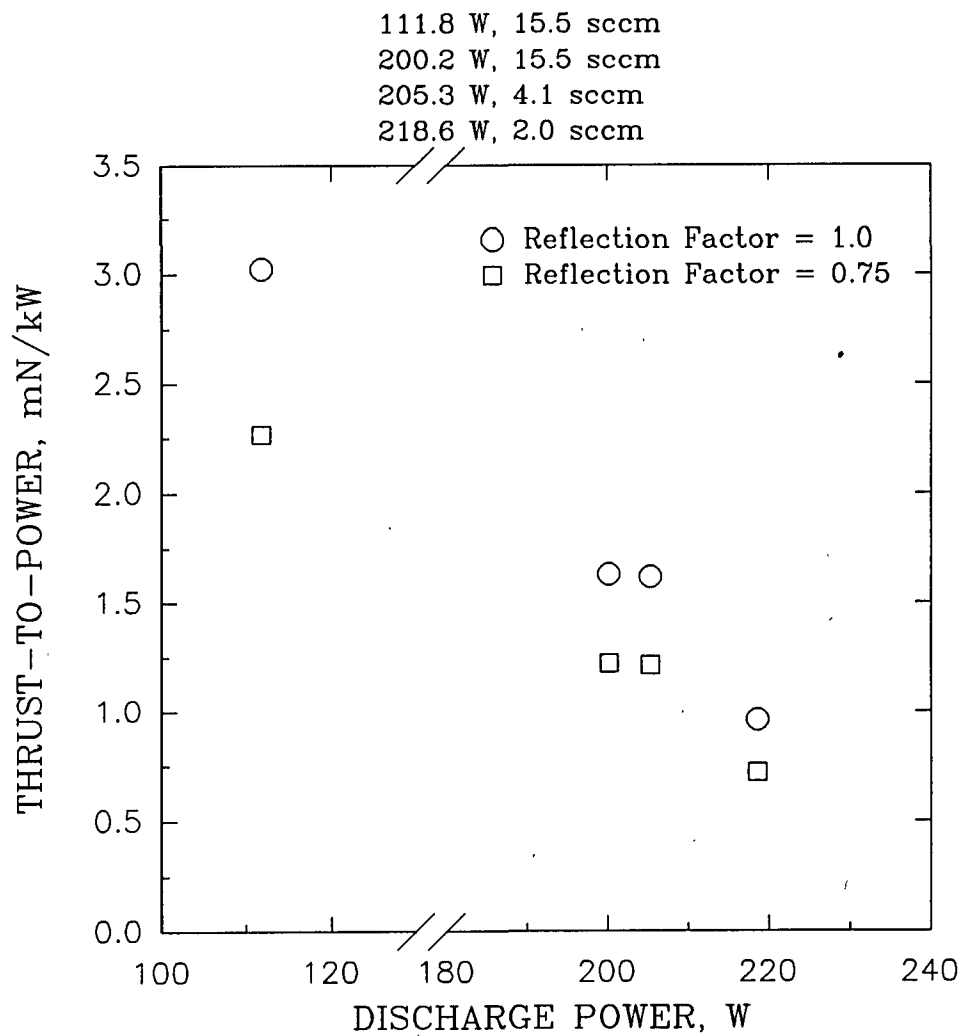


Fig. 27c
MEP Thruster Thrust-to-Power Characteristics with Cavity Anode

the hypothesis that the plasma acceleration mechanism depended more on the radial magnetic field component than the axial magnetic field component, since the second and less effective magnet position of $X = 5.4$ mm corresponded to placement of the emitter orifice, and cavity anode, in a predominately axially directed magnetic field.

Ring Anodes

Next, a series of parametric tests were performed wherein different MEP thruster geometries were investigated using ring permanent magnets, and a ring anode structure. The intent of these geometry choices was to promote plasma production in a predominately radial magnetic field region, while also increasing the volume of plasma production. With this configuration, better coupling of the input power to the propellant gas was anticipated. A total of ten MEP thruster ring anode configurations were investigated. All of these configurations shared a common emitter, radiation shield and primary ring magnet geometry, and these major components are shown in Figs. 28a, 28b and 28c. It should be noted from Fig. 28c that the large ring magnet, and emitter radiation shielding, were always exposed to the discharge plasma, and at cathode potential, unless otherwise noted. The large ring magnet was manufactured from Alnico 5-7 material, whose energy product is approximately 30% greater than Alnico 5.¹⁵ Figure 29 plots the measured axial magnetic field distribution for this ring magnet which was magnetized parallel to its axis. Comparing this field distribution plot with that for the smaller ring magnet shown in Fig. 22, shows that the use of more magnet material did have the desired effect of significantly increasing the measured field strength.

Figure 30 shows schematically the relative locations of the major MEP thruster components used during parametric testing of various ring anode geometries. Initial tests were performed using graphite ring anodes with inside diameters ranging from 22.2 mm to 10.7 mm. These test anodes were located approximately 9.0 mm from the MEP emitter orifice, in a region of strong, radially directed magnetic field. Figures 31a, 31b and 31c show this variation in anode hole diameter, and the method of affixing and isolating these anodes from the magnet and emitter. With a 22.2 mm dia. ring anode, the MEP thruster anode current could not be increased above 0.2 - 0.3 A, over a 50 - 100 sccm flow rate range, without causing the anode to glow red hot due to high anode voltages of order 60 - 70 V. This behavior was consistent with nearly complete magnetic shielding of the anode from the discharge plasma, which would create an electron accelerating plasma sheath in an attempt to satisfy the anode power supply current demand. Discharge currents of 0.3 A and less were too low to allow for MEP emitter self-heating. Reducing the ring anode diameter to 17.5 mm increased the anode current to 1.0 A, but anode voltages were still of order 50 - 60 V and the anode would glow red hot if flow rates were reduced below about 40 sccm. Tests with anode diameters of 14.7 mm and 10.7 mm, resulted in relatively low anode voltage operation, at

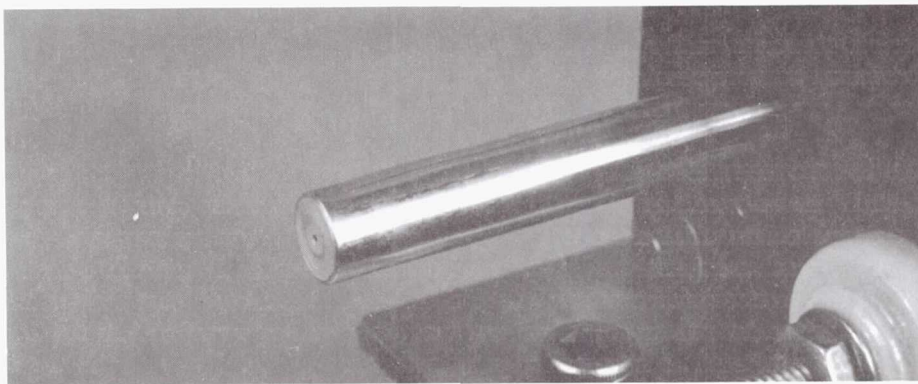


Fig. 28a
MEP Thruster Emitter at Start of Ring Anode Tests

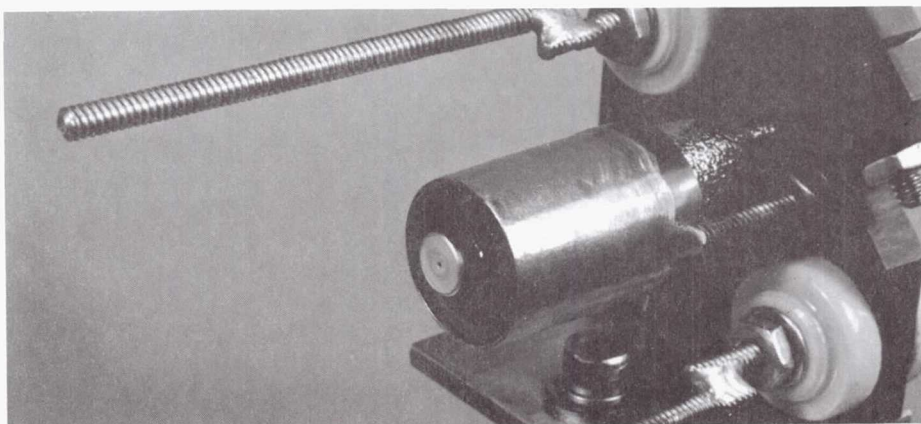


Fig. 28b
Radiation Shielding Added to Emitter

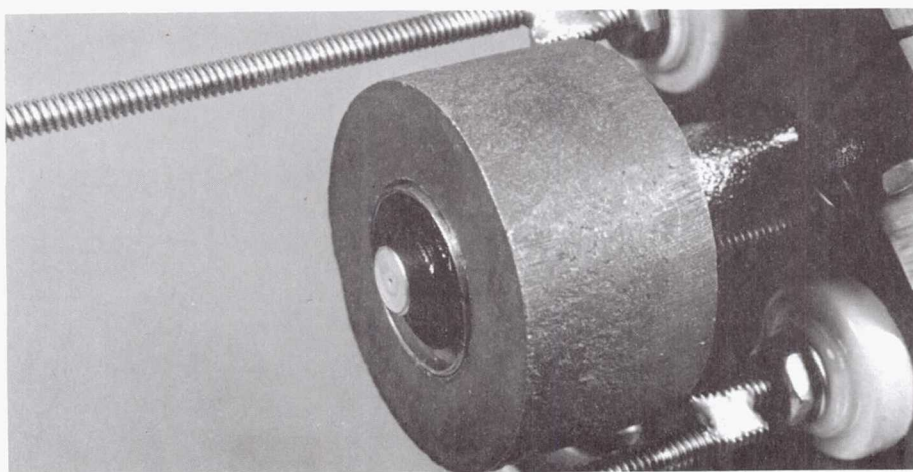


Fig. 28c
Large Alnico 5-7 Ring Magnet, Shown in Fully Retracted Position

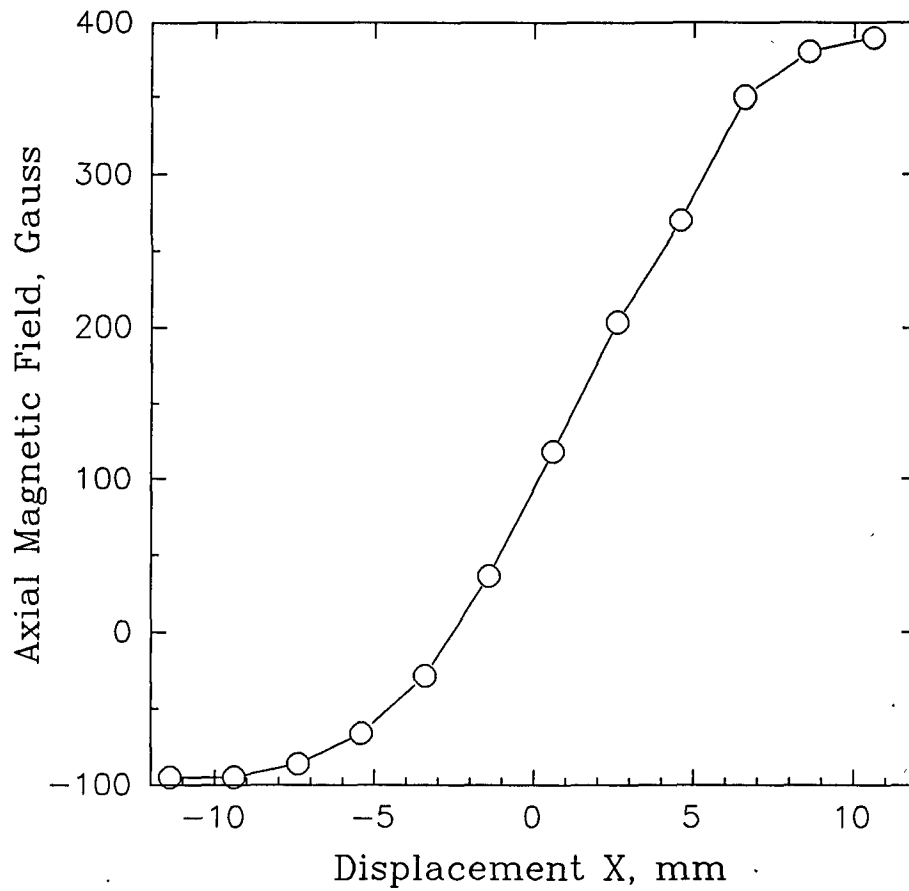
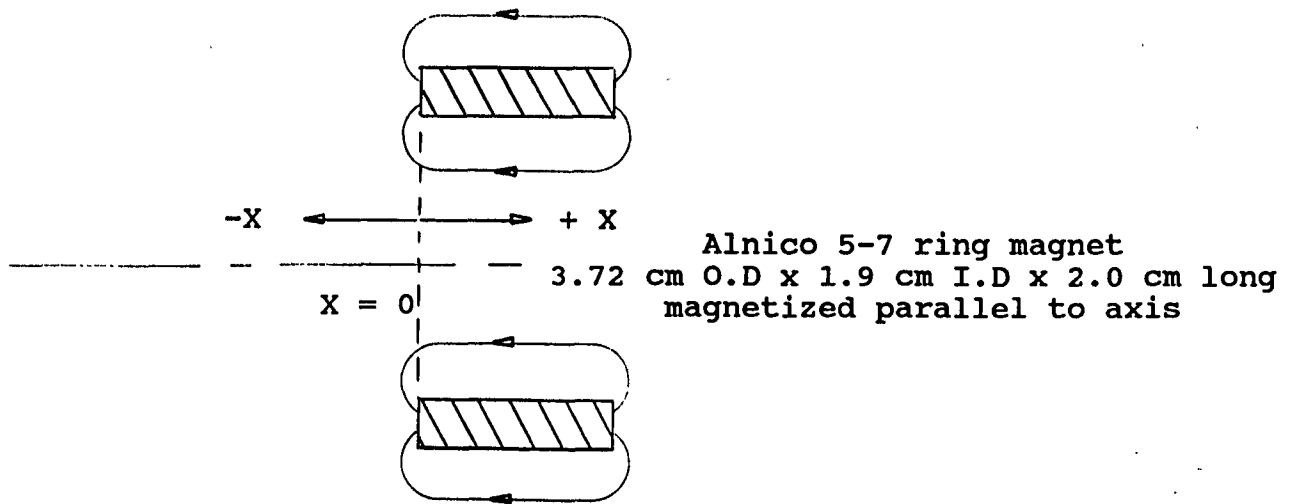


Fig. 29
Measured Axial Magnetic Field Distribution for Large Alnico 5-7
Ring Magnet Shown in Fig. 28c

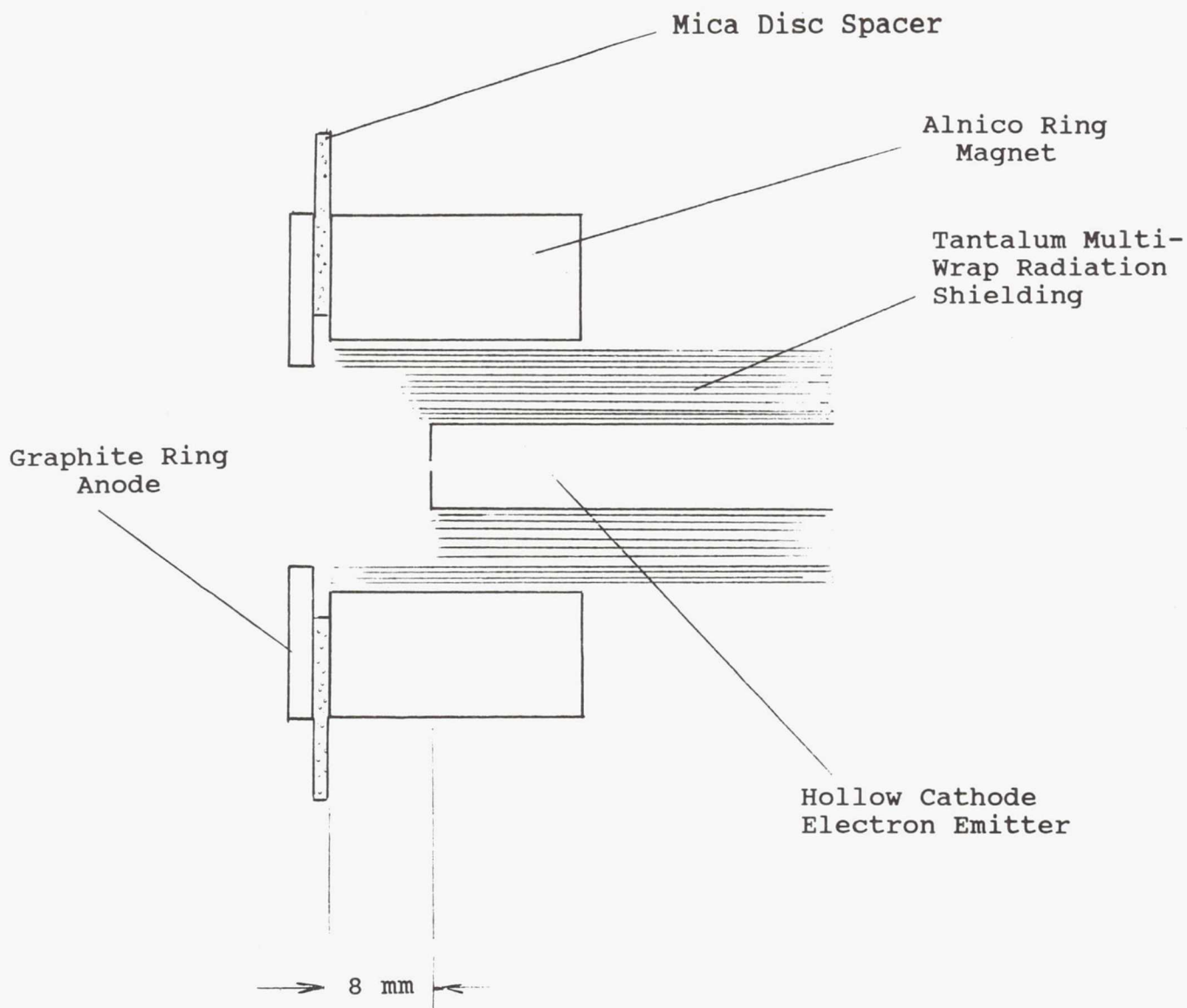


Fig. 30
Schematic Showing Relative Locations of Major Components During
Ring Anode Parametric Testing

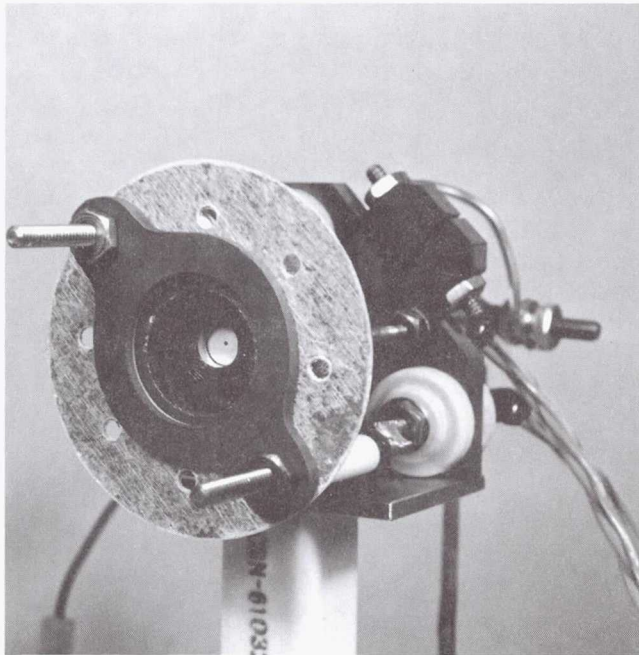


Fig. 31a
MEP Thruster Showing Largest
(22.2 mm dia.) Anode Tested

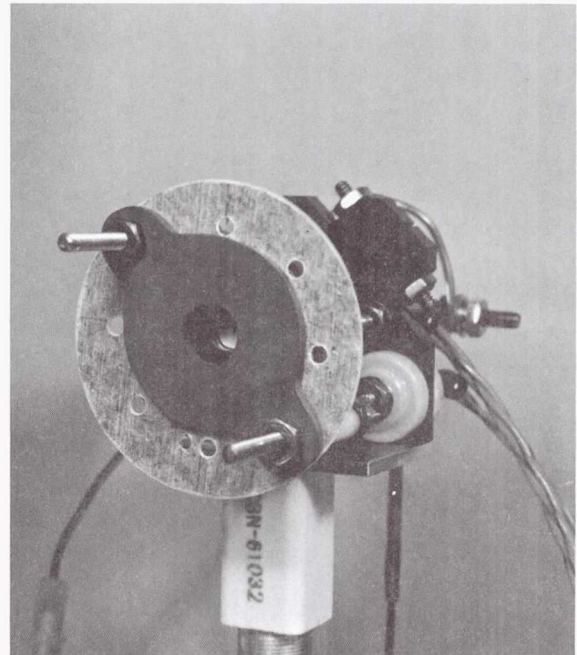


Fig. 31b
MEP Thruster Showing Smallest
(10.7 mm dia.) Anode Tested

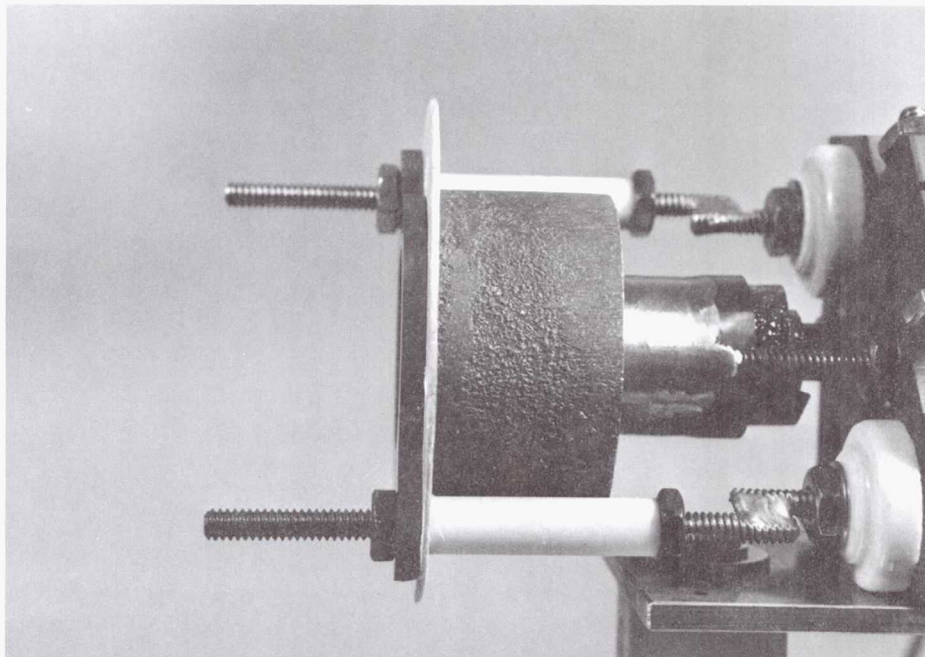


Fig. 31c
Side View of MEP Thruster Showing Mica Disc Used to Isolate
Graphite Ring Anodes From Cathode Biased Ring Magnet

low propellant flow rates, and with no apparent ring anode heating. Comparing measured performance showed generally better MEP thruster performance for the 14.7 mm dia. ring anode.

Proceeding with the most promising of these tested anodes, several MEP thruster configurations were assembled and operated using the 14.7 mm dia. graphite ring anode. The photographs in Figs. 32a - 32d summarize these different test configurations. Briefly, Figs. 32a and 32b show a configuration wherein an alumina tube was placed over the MEP emitter, extending up to the ring anode. The intent of this insulating tube was to prevent the discharge plasma from interacting with the cathode biased ring permanent magnet. Performance measurements indicated a significant drop in specific impulse and efficiency using this alumina tube. Furthermore, repeating these tests with the ring magnet and applied field direction reversed, did not appreciably alter the measured specific impulse and efficiency of this configuration.

Figure 32c shows the MEP thruster configured with a 50% open area stainless steel screen over the ring anode hole exit. The screen was allowed to float electrically and no magnet shielding alumina tube was used. Performance measurements indicated a drop in specific impulse and efficiency similar to that for the configuration in Figs 32a and 32b.

Figure 32d shows the MEP thruster configured with an additional thin ring magnet which was magnetized in the radial direction (no screen or alumina magnet shielding tube were used). This magnet had an inside diameter of 19.1 mm, an outside diameter of 31.8 mm and a thickness of 6.4 mm. The magnet was biased at anode potential and functioned as the MEP thruster anode. Performance measurements indicated higher specific impulse and efficiency than were achieved with the configurations shown in Figs. 32a and 32b and Fig. 32c. However, this measured performance was still less than originally obtained using only the single large ring magnet.

Final Test Geometry

Following testing and performance analysis of the configurations shown in Figs. 31 and 32, the MEP thruster was assembled according to the component specifications shown schematically in Fig. 33. Figures 34a - 34c show photographs of this final MEP thruster configuration. For this test configuration, careful attention was paid to eliminating any propellant gas leakage except through the ring anode, and to improve the emitter thermal efficiency by applying more radiation shielding. It should be noted that Fig. 34c actually shows details of the emitter orifice after all Phase I testing had been completed. Inspection of this figure shows that very little erosion occurred during the approximately 30 hours of operation accumulated during this program. The little emitter orifice plate erosion evident in Fig. 34c was believed to have been caused during testing at very high discharge currents up to 7.0

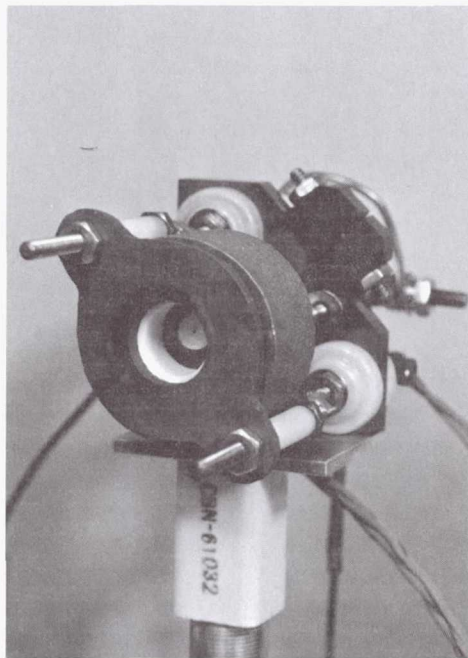


Fig. 32a
MEP Thruster with Alumina
Tube Isolating Magnet
Walls From Plasma

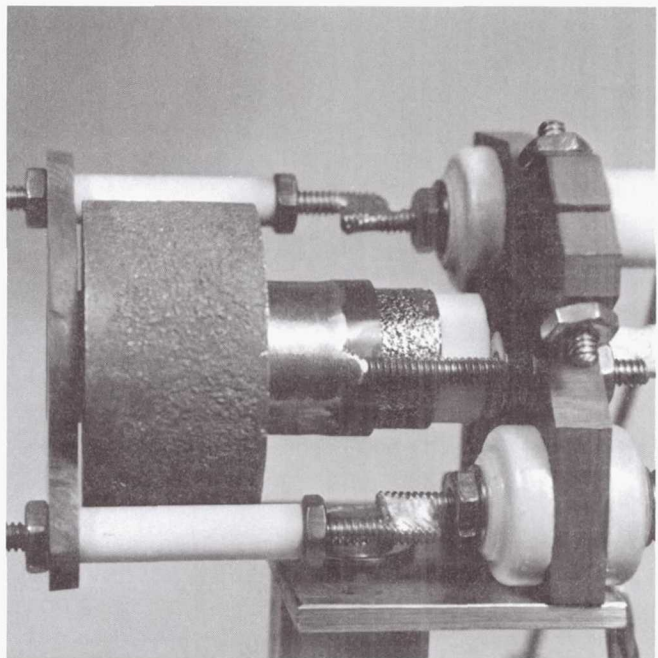


Fig. 32b
Side View of MEP Thruster
Showing Alumina Tube Extended
Over Entire Emitter Length

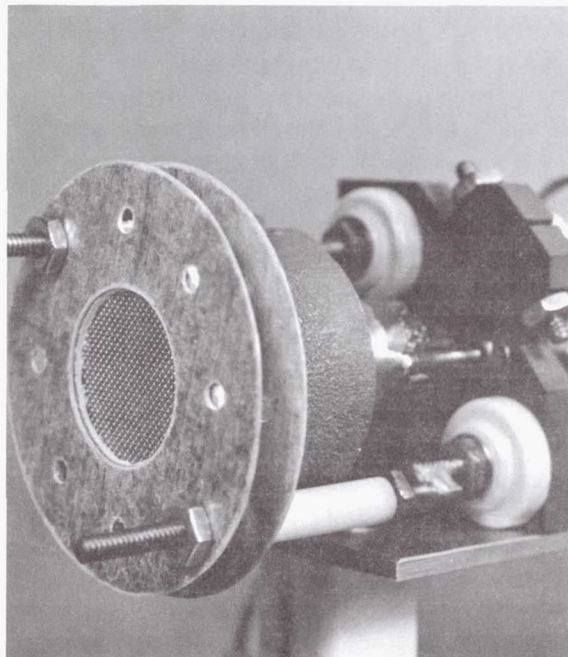


Fig. 32c
MEP Thruster Ring Anode
Exit Fitted with a
Floating (50% Open Area) Screen

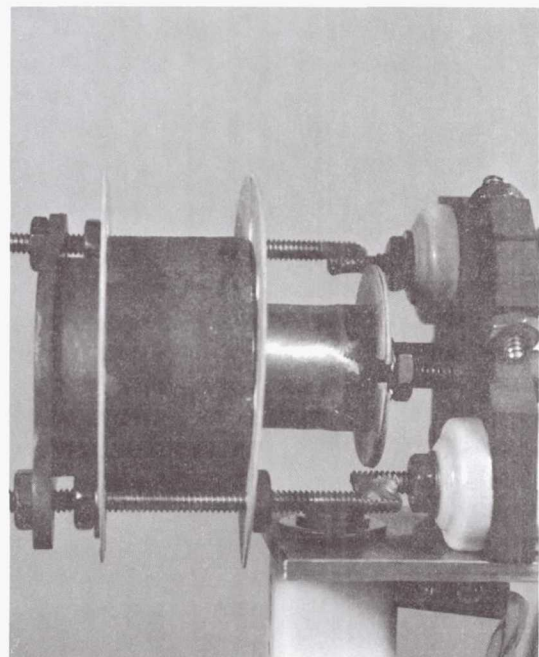


Fig. 32d
MEP Thruster Fitted with a
Radially Magnetized Ring Magnet
Acting as an Anode

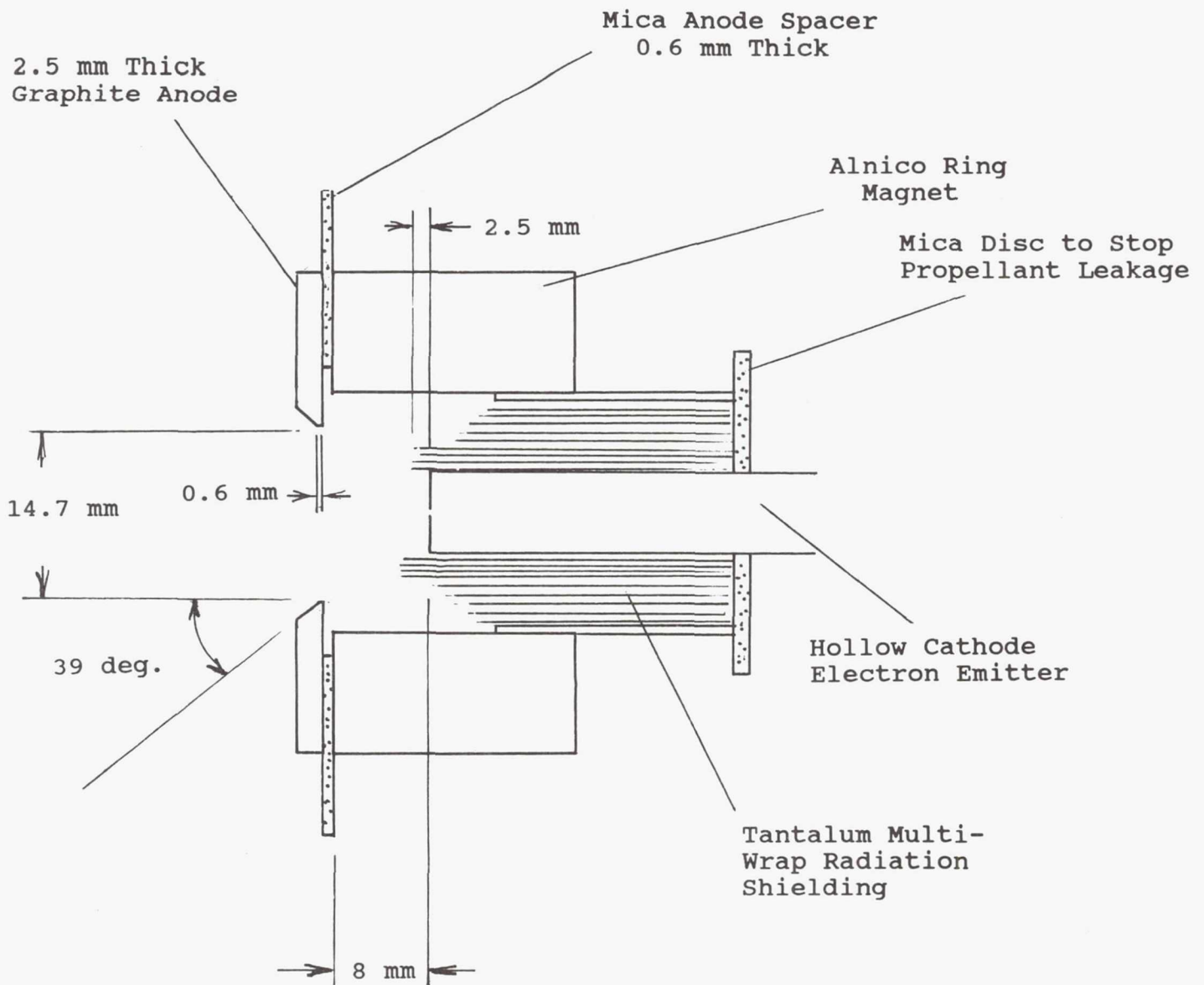


Fig. 33
Design Details of Final Ring Magnet MEP Thruster Configuration

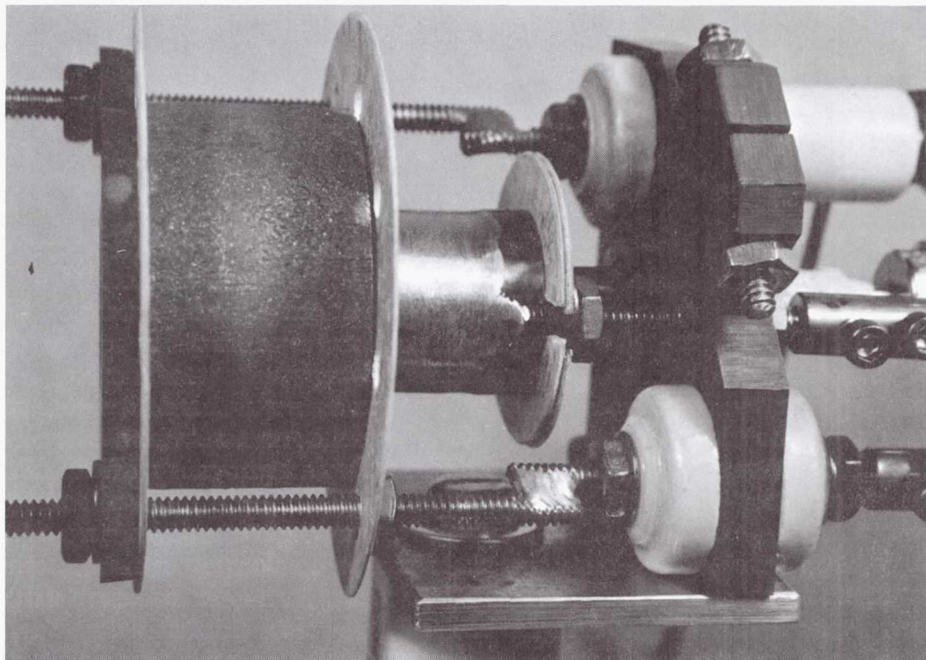


Fig. 34a
MEP Thruster Side View showing Additional Mica Discs to Reduce
Propellant Leakage and Radiative Heat Loss

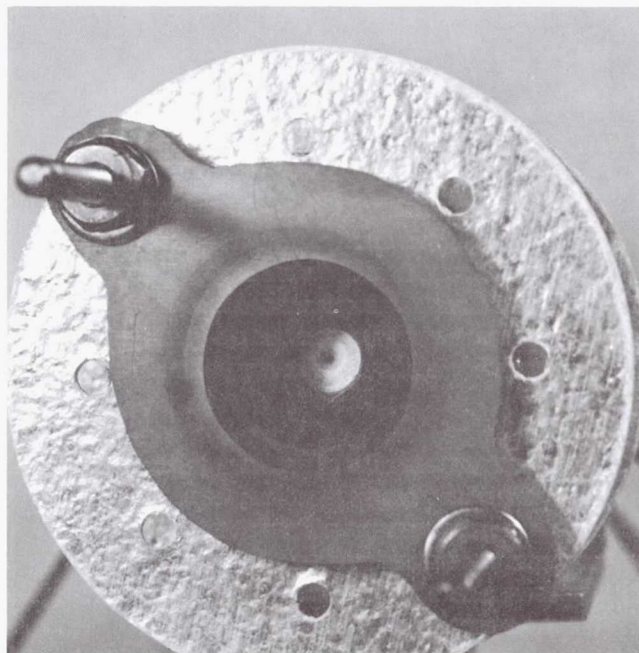


Fig. 34b
MEP Thruster Front View

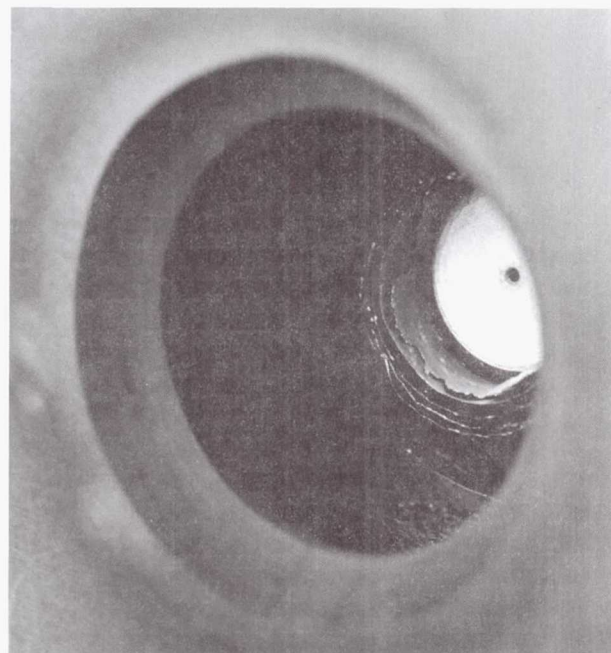


Fig. 34c
Detail of MEP Thruster Discharge
Chamber Showing Chamfered Anode
and Emitter Radiation Shielding

A, as noted in Figs. 24 and 25.

Figure 35 documents the discharge starting characteristics of the MEP thruster configuration shown in Figs. 33 and 34 as a function of propellant flow rate for a constant starting insert heater current of 16.0 A. It is important to note in Fig. 35 that MEP thruster start-up with the ring anode configuration did not require a gas or high voltage pulse, and that discharge initiation occurred every time by turning up the anode power supply voltage. Starting voltage requirements for this final MEP thruster test geometry did not vary by more than $\pm 5\%$ from the values plotted in Fig. 35.

Typically, the MEP emitter insert heater was turned off within ten seconds after the discharge was initiated. After this heater was turned off, the emitter insert temperature was sustained by self-heating due to ion bombardment from the discharge plasma. Figure 36 plots the voltage and current characteristics of the final MEP thruster configuration as a function of propellant flow rate. These data illustrate that the device had a well behaved negative impedance characteristic.

Figure 37 shows the MEP thruster plume and plots the measured plume thrust density distribution for MEP thruster operation at a constant flow rate of 20 sccm. These data show that a vigorous plasma acceleration process was operating in the MEP thruster discharge. This result is especially remarkable because, in the discharge only mode where the insert heater was off, a significant fraction of the discharge power is required to self-heat the insert, and thus sustain the electron emission process. EPL estimates that approximately 10 - 15 watts of discharge power are required to self-heat the emitter insert. This power requirement would be expected to be reduced significantly with thermal design improvements to the MEP thruster.

Figures 38a - 38c summarize the measured performance characteristics of the final MEP thruster ring anode configuration that was examined. The data in Fig. 38c show a large increase in thrust-to-power for the ring anode MEP thruster configuration, as compared to the cavity anode configuration shown in Fig. 27d.

Thrusting Mechanism

Figure 39 shows a schematic representation of the MEP thruster and illustrates the acceleration mechanism which EPL theorizes is operating within the discharge plasma. Briefly, ion acceleration is theorized to occur because of predominately axial voltage gradients formed across a high plasma impedance magnetic bottle. Cathode electrons trapped in this bottle generate these accelerating electric fields as they ionize neutral propellant atoms, while working their way across these applied magnetic field lines to the anode. Due to the predominately axial magnetic field distribution at the emitter

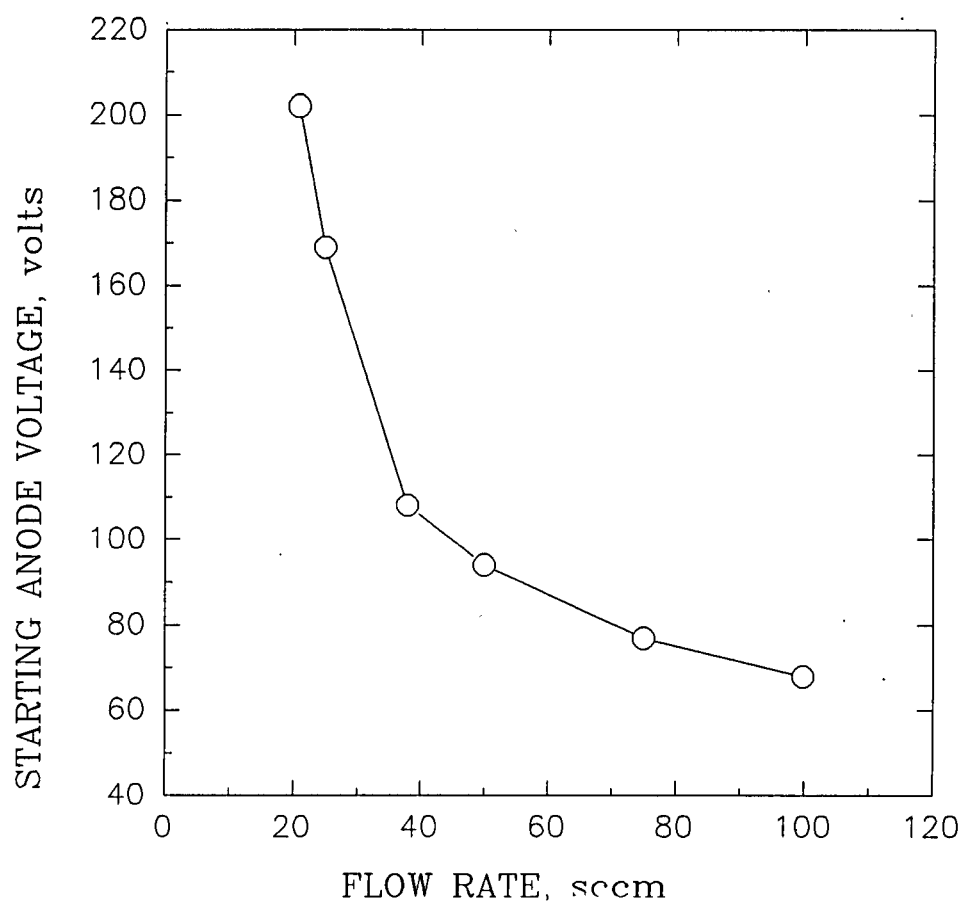


Fig. 35
MEP Thruster Starting Voltage Dependence on Flow Rate for Final
Ring Anode Configuration

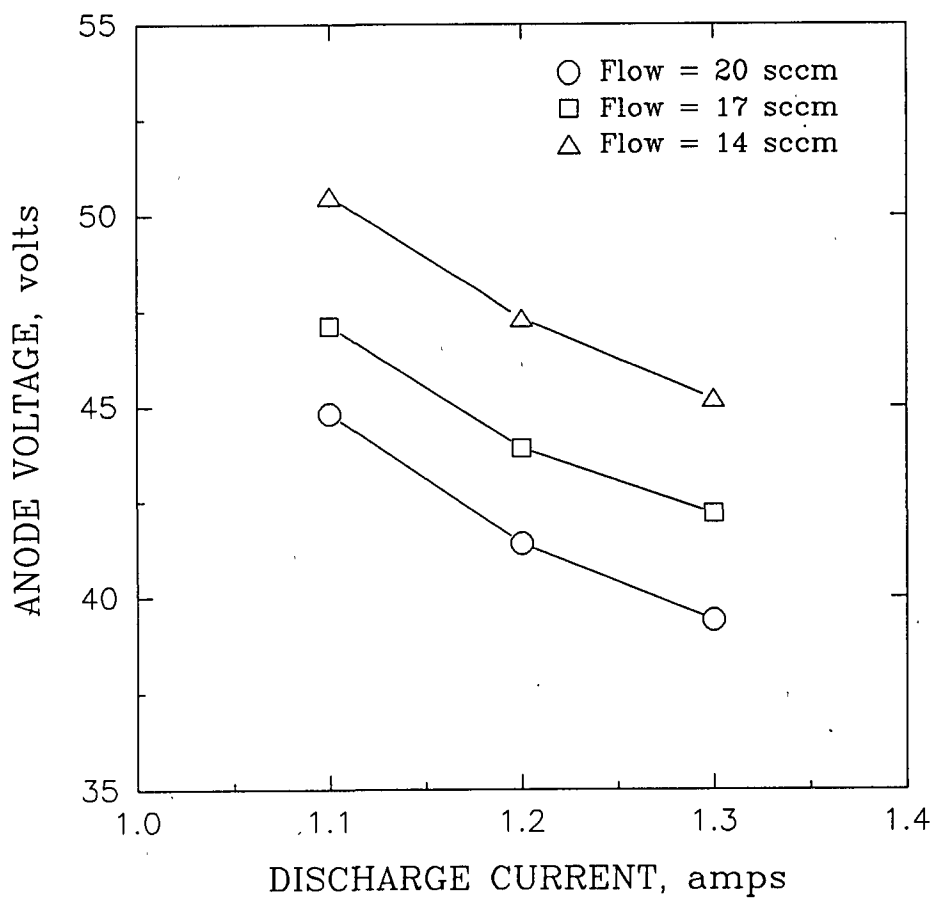


Fig. 36
MEP Thruster Voltage and Current Characteristics with Emitter Self-Heating

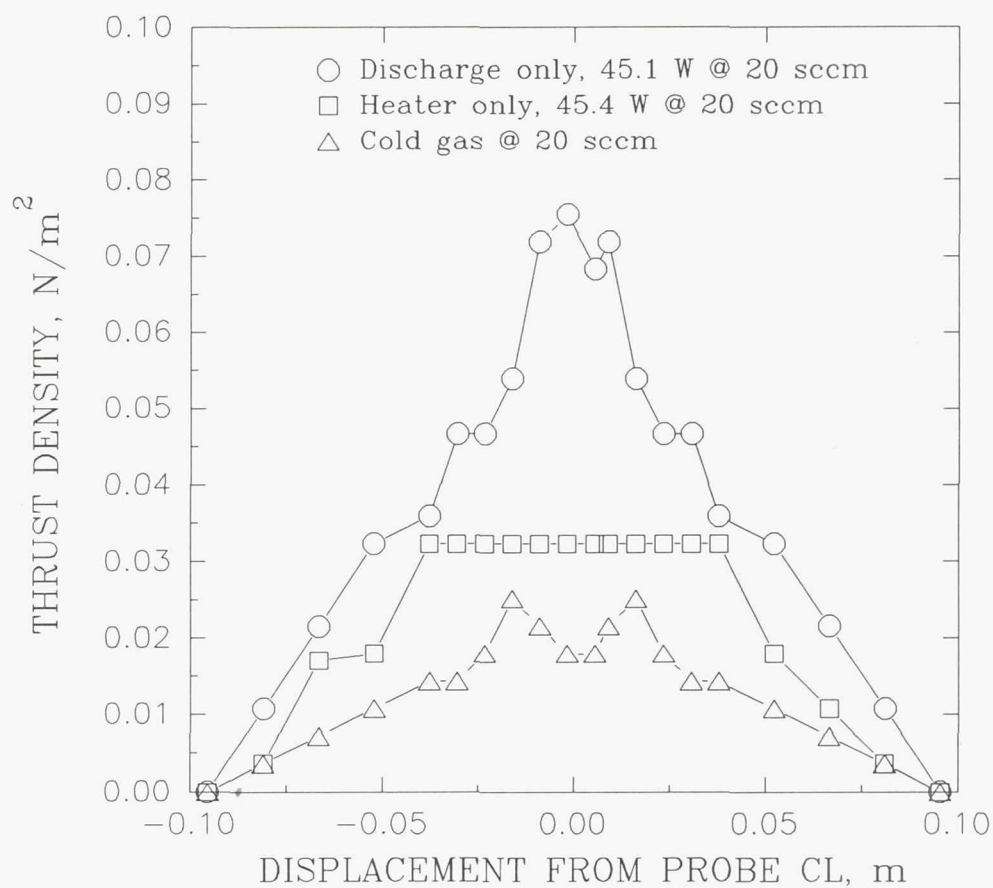
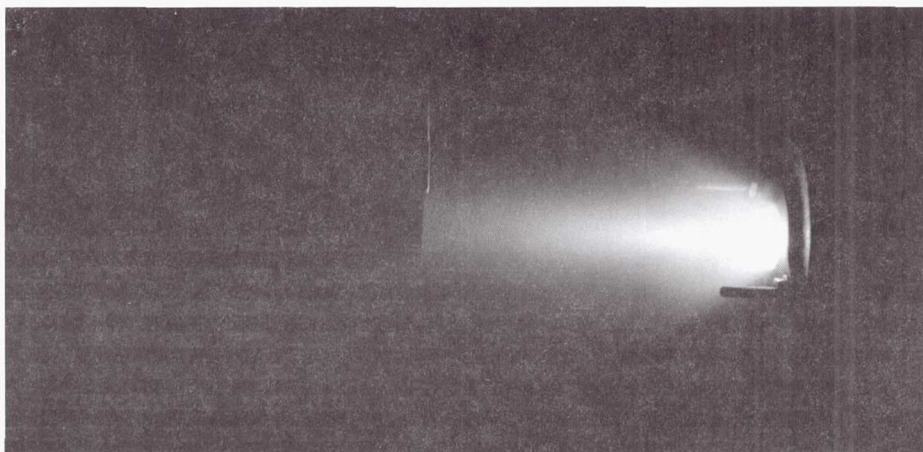


Fig. 37
Typical Plume Characteristics of Final MEP Thruster Configuration
and Thrust Density Plots Corresponding to Various Thruster
Operating Modes

45.1 W : 39.55 volts @ 1.14 amps, 20 sccm
54.8 W : 42.15 volts @ 1.3 amps, 20 sccm
59.6 W : 47.1 volts @ 1.27 amps, 14 sccm

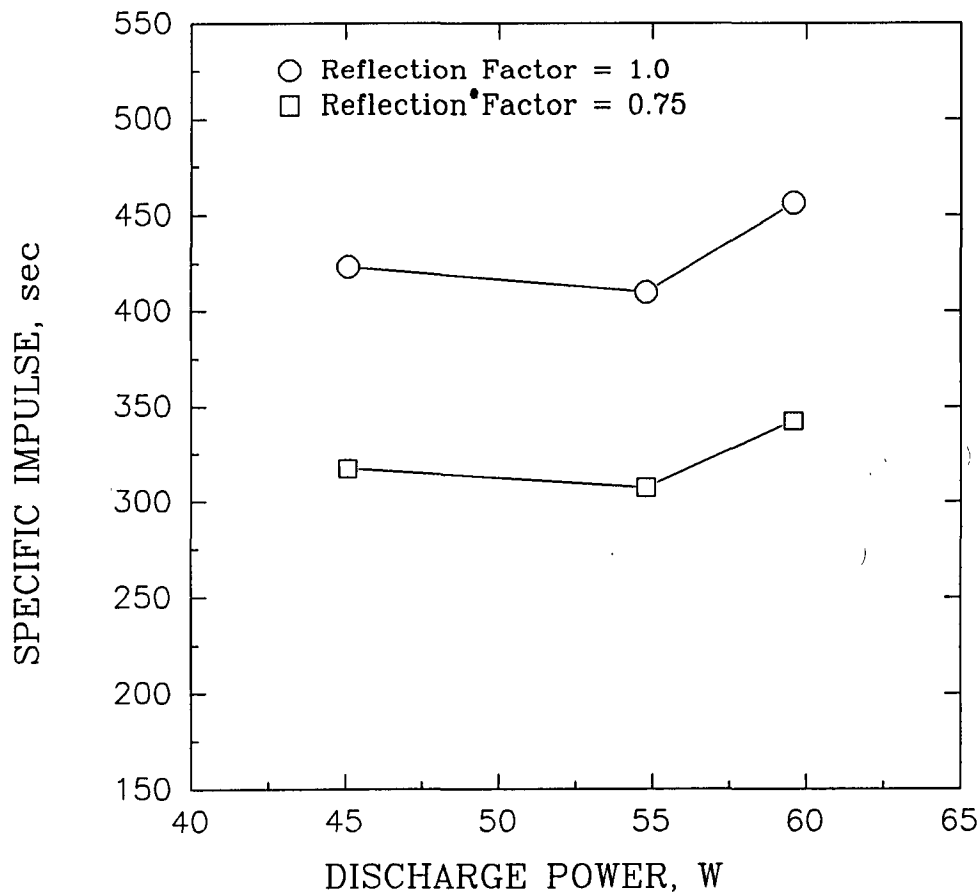


Fig. 38a
Specific Impulse Characteristics of Final MEP Thruster Configuration

45.1 W : 39.55 volts @ 1.14 amps, 20 sccm
54.8 W : 42.15 volts @ 1.3 amps, 20 sccm
59.6 W : 47.1 volts @ 1.27 amps, 14 sccm

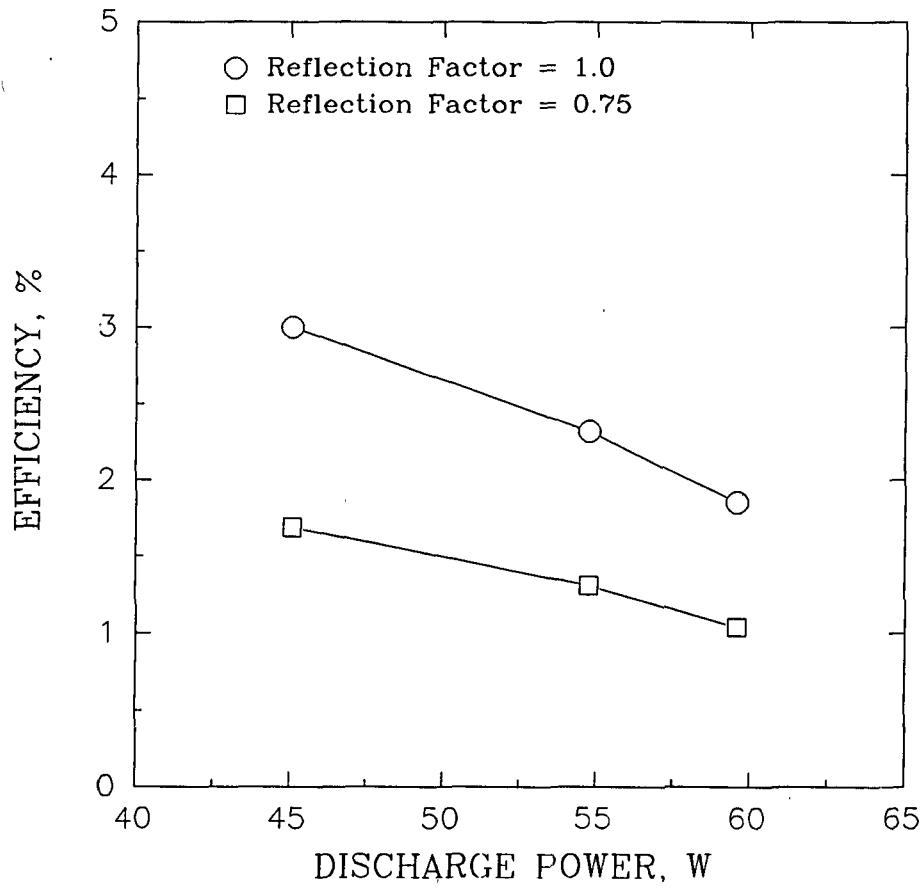


Fig. 38b
Efficiency Characteristics of Final MEP Thruster Configuration

45.1 W : 39.55 volts @ 1.14 amps, 20 sccm
54.8 W : 42.15 volts @ 1.3 amps, 20 sccm
59.6 W : 47.1 volts @ 1.27 amps, 14 sccm

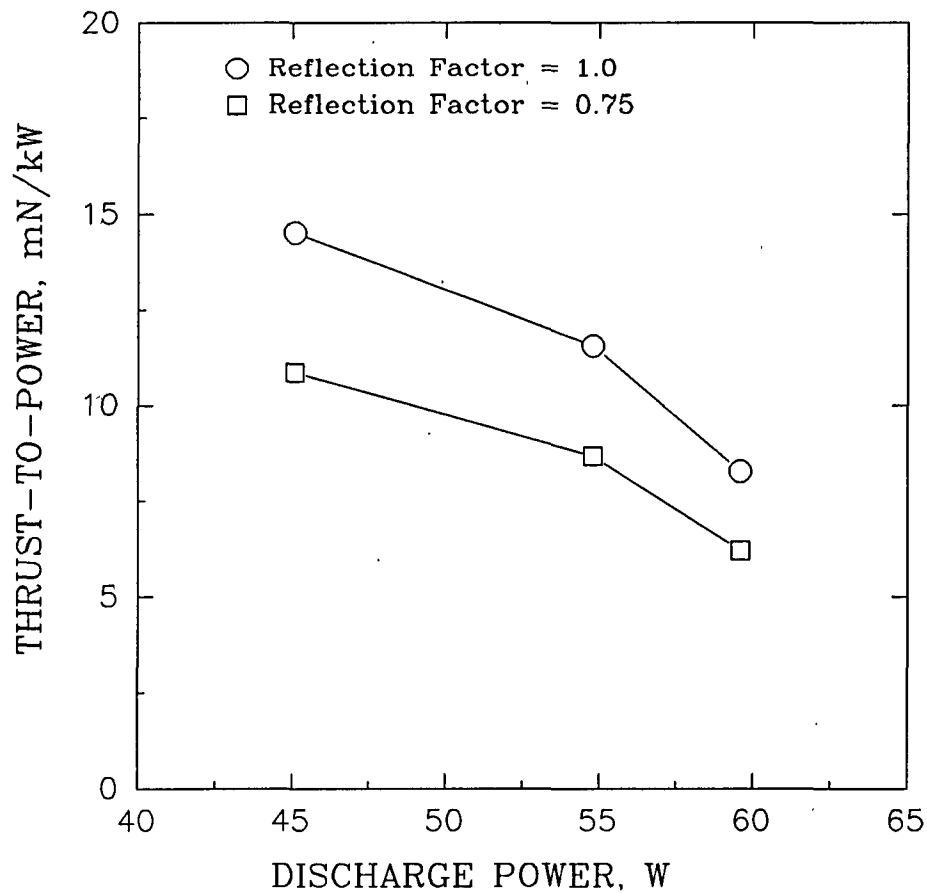


Fig. 38c
Thrust-to-Power Characteristics of Final MEP Thruster Configuration

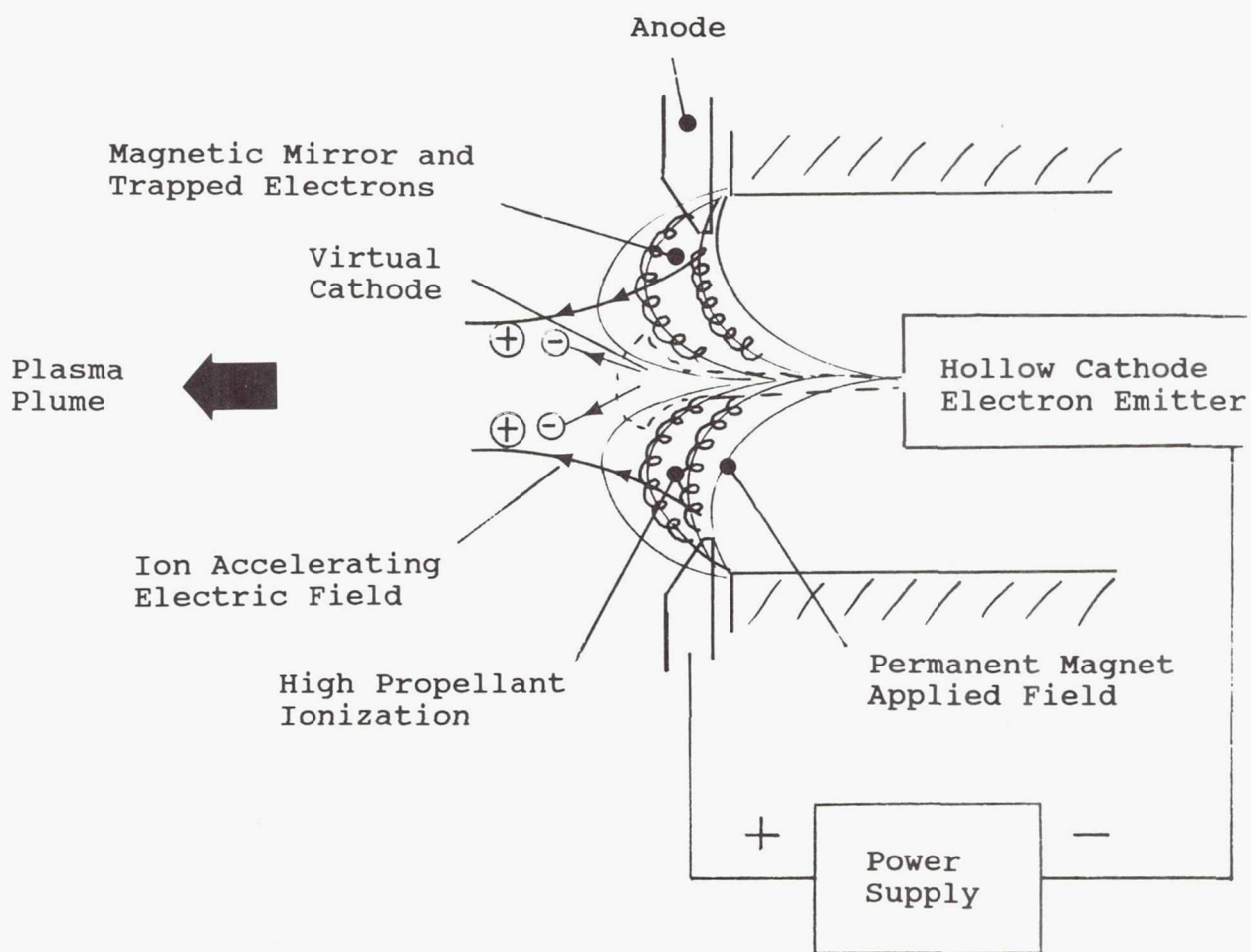


Fig. 39
Schematic Representation of Theorized MEP Thruster Plasma
Acceleration Mechanism

orifice, a virtual cathode is hypothesized to form along the device centerline. This virtual cathode is theorized to supply low energy electrons to space-charge neutralize the accelerated ions as they leave the MEP thruster.

CONCLUSIONS

This Phase I program has developed a new plasma acceleration process which has been shown capable of providing useful thrust and specific impulse for a miniature plasma accelerator in the power regime below 50 W. Although specific impulse levels as high as 1,000 sec. were attained during this program using a cavity anode, parametric thruster geometry changes showed that the most efficient plasma acceleration was achieved with a ring anode and ring magnet geometry. Proof-of-concept tests with this ring anode MEP thruster configuration, operating on a 33% N_2 \ 67% H_2 propellant mixture (ie. simulated hydrazine), demonstrated a specific impulse of order 350 - 400 sec., at a thrust-to-power ratio of about 12 mN/kW, for a total input power of 45 W and using only one power supply. In addition to these very good preliminary performance measurements, reliable start-up was demonstrated at an applied voltage of only a few tens of volts. Similarly, no excessive or unusual thruster erosion behavior occurred during testing on the simulated hydrazine propellant mixture, which included approximately one hundred and fifty starts and thirty hours of accumulated thruster operation.

The plasma acceleration mechanism discovered during this program was found to depend on several key parameters which included: the propellant flow rate, the geometry of the applied magnetic field, the anode geometry and location, the electron emission efficiency of the emitter, and the volume of the discharge chamber. Furthermore, these Phase I proof-of-concept investigations demonstrated the extreme sensitivity of MEP thruster performance to changes in these parameters. A preliminary hypothesis describing the plasma acceleration process was presented. It is apparent that the ultimate assessment of MEP thruster performance requires substantial optimization testing; a fact well proven by other electric propulsion technologies.

It is the recommendation of EPL that the SDIO/IST support a Phase II proposal directed toward the demonstration of a performance optimized MEP thruster for miniature spacecraft applications using the new plasma acceleration mechanism discovered during this successful Phase I program.

REFERENCES

1. Whitehead, J. C., Swink Jr., D. G. and Toews, H. G., "Pumped Hydrazine Miniaturized Propulsion System", AIAA Paper No. 89-2958, July 1989.
2. Whitehead, J. C., "Free Piston Pumps for Miniature Rocket Propulsion", AIAA Paper No. 91-1837, June 1991.
3. Aston, G. and Acker T. L., "Preliminary Tests of the Electrostatic Plasma Accelerator", AIAA Paper No. 90-2596, July 1990.
4. Aston, G. and Aston, M. B., "Momentum Probe for Low Thrust Measurement", AIAA Paper No. 91-2563, June 1991.
5. Carta, D. G., "Problems of Millipound Thrust Measurement - the Hansen Suspension", AIAA Paper No. 63-034, March 1963.
6. Kami, S. and Herron, B. G., "An Ion Engine Thrust Vector Measuring Device", AIAA Paper No. 70-1104, Sep. 1970.
7. Snyder, A. and Banks, B. A., "Thrust Measurements of a Hollow Cathode Discharge", NASA TN D-6705, 1972.
8. Murch, C. K., Broadwell, J. E., Silver, A. H. and Marcisz, T. J., "Performance Losses in Low Reynolds Number Nozzles", J. Spacecraft, Vol. 5, No. 9, Sep. 1968.
9. Holcomb, L. B., "Satellite Auxiliary-Propulsion Selection Techniques", JPL Technical Report 32-1505, Nov. 1970.
10. Curran, F. M., Sovie, A. J. and Haag, T. W., "Arcjet Nozzle Design Impacts", NASA TM 102050, May 1989.
11. Aston, G. and Brophy, J. R., "An Annular Ion Accelerator System for Large Diameter, High Thrust ION Engines", EPL-DOC-88-103, prepared for Contract Nos. NAS3-25207 and NAS3-25267, May 1988. Also appears in: Aston, G. and Brophy, J. R., "A 50 cm Diameter Annular Ion Engine", AIAA Paper No. 89-2716, July 1989.
12. Aston, G. and Acker, T. L., "Electrostatic Plasma Accelerator", EPL-DOC-90-100, prepared under SubContract CAR\EPL 89-01 for the Center for Advanced Space Propulsion, July 1990.
13. Aston, G., "Electrostatic Plasma Accelerator for Small Satellites", Final Report No. EPL-DOC-91-100. Prepared for Contract No. DAAH01-90-0601 for the Defense Advanced Research Projects Agency, Jan. 1991.
14. Zafran, S. and Jackson, B., "Electrothermal Thruster Diagnostics", NASA CR-168174, May 1983.

15. The Dexter Corporation: Magnet Materials Division.
Permanent Magnet Product Catalog P5A, 1989.

REPORT DOCUMENTATION PAGE			Form Approved OMB No. 0704-0188	
Public reporting burden for this collection of information is estimated to average 1 hour per response, including the time for reviewing instructions, searching existing data sources, gathering and maintaining the data needed, and completing and reviewing the collection of information. Send comments regarding this burden estimate or any other aspect of this collection of information, including suggestions for reducing this burden, to Washington Headquarters Services, Directorate for Information Operations and Reports, 1215 Jefferson Davis Highway, Suite 1204, Arlington, VA 22202-4302, and to the Office of Management and Budget, Paperwork Reduction Project (0704-0188), Washington, DC 20503.				
1. AGENCY USE ONLY (Leave blank)		2. REPORT DATE November 1992		3. REPORT TYPE AND DATES COVERED Final Contractor Report
4. TITLE AND SUBTITLE Micro Electric Propulsion Feasibility			5. FUNDING NUMBERS WU-506-42-31	
6. AUTHOR(S) Graeme Aston and Martha Aston				
7. PERFORMING ORGANIZATION NAME(S) AND ADDRESS(ES) Electric Propulsion Laboratory, Inc. 440 N. Green Street Tehachapi, CA 93561			8. PERFORMING ORGANIZATION REPORT NUMBER E-7428	
9. SPONSORING/MONITORING AGENCY NAMES(S) AND ADDRESS(ES) National Aeronautics and Space Administration Lewis Research Center Cleveland, Ohio 44135-3191			10. SPONSORING/MONITORING AGENCY REPORT NUMBER NASA CR-189139	
11. SUPPLEMENTARY NOTES Project Manager, John M. Sankovic, (216) 977-7429.				
12a. DISTRIBUTION/AVAILABILITY STATEMENT LIMITED DISTRIBUTION DOCUMENT Because of its significant technological potential, this information which has been developed under a U.S. Government program is being given a limited distribution whereby advanced access is provided for use by domestic interests. This legend shall be marked on any reproduction of this information in whole or in part. Date for general release November 1994 Subject Category 20			12b. DISTRIBUTION CODE	
13. ABSTRACT (Maximum 200 words) Miniature, 50 kg class, strategic satellites intended for extended deployment in space require an on-board propulsion capability to perform needed attitude control adjustments and drag compensation maneuvers. Even on such very small spacecraft, these orbit maintenance functions can be significant and result in a substantial propellant mass requirement. Development of advanced propulsion technology could reduce this propellant mass significantly, and thereby maximize the payload capability of these spacecraft. In addition, spacecraft maneuverability could be enhanced and/or multi-year mission lifetimes realized. These benefits cut spacecraft replacement costs, and reduce services needed to maintain the launch vehicles. For SDIO brilliant pebble spacecraft, a miniaturized hydrazine propulsion system provides both boost and divert thrust control. This type of propulsion system is highly integrated and is capable of delivering large thrust levels for short time periods. However, orbit maintenance functions such as drag make-up require only very small velocity corrections. Using the boost and/or divert thrusters for these small corrections exposes this highly integrated propulsion system to continuous on/off cycling and thereby increases the risk of system failure. Furthermore, since drag compensation velocity corrections would be orders of magnitude less than these thrusters were designed to deliver, their effective specific impulse would be expected to be lower when operated at very short pulse lengths. The net result of these effects would be a significant depletion of the on-board hydrazine propellant supply throughout the mission, and a reduced propulsion system reliability, both of which would degrade the interceptor usefulness. In addition to SDIO brilliant pebble spacecraft, comparably small spacecraft can be anticipated for other future strategic defense applications such as surveillance and communication. For such spacecraft, high capability and reliability, minimal detectability and low cost are requirements. All these miniature spacecraft share a common characteristic: because of their on-board electronic equipment they have, by design, solar order 50-100 W. In a relative sense, such spacecraft are power rich when compared to other larger spacecraft. This power rich situation is offset by very tight mass budgets, which make reductions in propellant mass requirements a key issue in meeting overall spacecraft minimum mass goals. In principle, power rich and propellant poor brilliant pebbles class spacecraft can benefit from using high specific impulse electric propulsion to reduce chemical propellant mass requirements. However, at power levels of order 50 W, arcjets cannot be made to function, ion thrusters are too complex and heavy, and resistojets have too low a specific impulse. Recognizing these capability limitations in existing electric propulsion technology, the SDIO/IST sponsored the Phase I SBIR Micro Electric Propulsion (MEP) thruster study described in this report. The objective of this study was to examine the feasibility of developing a very simple, low mass and small volume, electric thruster for operation on hydrazine at less than 100 W of input power. The feasibility of developing such a MEP thruster was successfully demonstrated by EPL by the discovery of a novel plasma acceleration process. The following sections in this report summarize the approach, test results and major accomplishments of this proof-of-concept program.				
14. SUBJECT TERMS Electric propulsion; Micro thrusters; Hollow cathodes			15. NUMBER OF PAGES 73	
			16. PRICE CODE A04	
17. SECURITY CLASSIFICATION OF REPORT Unclassified	18. SECURITY CLASSIFICATION OF THIS PAGE Unclassified	19. SECURITY CLASSIFICATION OF ABSTRACT Unclassified	20. LIMITATION OF ABSTRACT	

National Aeronautics and
Space Administration

Lewis Research Center
Cleveland, Ohio 44135

Official Business
Penalty for Private Use \$300

FOURTH CLASS MAIL

ADDRESS CORRECTION REQUESTED



Postage and Fees Paid
National Aeronautics and
Space Administration
NASA 451

NASA
